Efficient and Accurate Sampling of the Thermal Neutron Scattering Law in OpenMC

by

Amelia J. Trainer

SUBMITTED TO THE DEPARTMENT OF NUCLEAR SCIENCE AND ENGINEERING IN PARTIAL FULFILLMENT OF THE REQUIREMENTS FOR THE DEGREES OF

~~BACHELOR OF SCIENCE IN NUCLEAR SCIENCE AND ENGINEERING~~

~~AND~~

MASTER OF SCIENCE IN NUCLEAR SCIENCE AND ENGINEERING

AT THE

MASSACHUSETTS INSTITUTE OF TECHNOLOGY

JUNE 2019

Signature of Author: Signature redacted

Amelia J. Trainer

Department of Nuclear Science and Engineering

May 18, 2019

Certified by: Signature redacted

Benoit Forget

Associate Professor of Nuclear Science and Engineering

Thesis Supervisor

Certified by: Signature redacted

Kord Smith

Korea Electric Power Company (KEPCO) Professor of the Practice of Nuclear Science and Engineering

Thesis Reader

Accepted by: Signature redacted

Ju Li

Battelle Energy Alliance Professor of Nuclear Science and Engineering and Professor of Materials Science and Engineering

Chair, Department Committee on Graduate Theses

Efficient and Accurate Sampling of the Thermal Neutron Scattering Law in OpenMC

by

Amelia J. Trainer

Submitted to the Department of Nuclear Science and Engineering on May 18, 2019 in Partial Fulfillment of the Requirements for the Degrees of Bachelor or Science in Nuclear Science and Engineering and Master of Science in Nuclear Science and Engineering

ABSTRACT

Convenient access to accurate nuclear data, particularly data describing low-energy neutrons, is crucial to the quality of thermal nuclear reactor simulations. Obtaining the scattering kernel for thermal neutrons (i.e. neutrons with energy on the order of 1 eV or less) can be a difficult problem, since the neutron energy is not enough to break molecular bonds, and thus the neutrons must often interact with a molecule or lattice structure. The "scattering law" $S(\alpha, \beta)$, which is a function of unitless momentum and energy transfer, is used to relate the frequency distribution (also called "vibrational density of states") of the scattering media, to the scattering kernel. Currently, the most popular method of calculating $S(\alpha, \beta)$ involves running the LEAPR module of the NJOY nuclear data processing code. Several antiquated approximations are used in LEAPR, such as the Einstein-crystal approximation (i.e. discrete oscillator approximation), which represents peaks in the frequency distribution as δ-functions. This project identifies insufficiencies in current thermal scattering data preparation: redundant numerical operations, arbitrary summation cutoffs, the discrete oscillator approximation, and the requirement that input frequency distributions be provided on a uniform energy mesh. Solutions to these shortcomings are identified and discussed. Additionally, a recently developed method of sampling energies and angles of the scattered neutrons is implemented into the OpenMC Monte Carlo neutron transport code to facilitate the testing of better phonon representations and maintain the continuous representation of the scattering kernel in energy and angle.

Thesis Supervisor: Benoit Forget

Title: Associate Professor of Nuclear Science and Engineering

Thesis Reader: Kord Smith

Title: Korea Electric Power Company (KEPCO) Professor of the Practice of Nuclear Science and Engineering

Acknowledgements

This work was made possible through support and collaboration with the nuclear data team XCP-5 at Los Alamos National Laboratory. This research made use of the NJOY nuclear data preparation code, which is maintained at Los Alamos.

First and foremost, I would like to extend my deepest thanks to my advisor, Prof. Ben Forget. In the fall of my freshman year, Prof. Forget gave me my first research experience, and since then he has provided unwavering support and insightful guidance, in both classes and research alike.

Additionally, I would like to thank members of the nuclear data team at LANL, particularly Dr. Jeremy Conlin, Austin McCartney, Dr. Denise Neudecker, and Dr. Wim Haeck. These inspiring individuals have not only mentored me and helped me gain technical skills, but have also shown me the joys of nuclear data processing, an area that I am excited to further explore.

I would also like to express my sincere gratitude to my "nuclear family" in the Nuclear Science and Engineering Department, and to my close friends who have provided both moral and technical support. Finally, I would like to thank my cats, Monster and Jacques-Gustav-Pierre, who are my rock.

Contents

List of Figures

List of Tables

Chapter 1

Introduction

1.1 Motivation

The accuracy of a nuclear system simulation is heavily dependent on the quality of the input nuclear data. Nuclear data (such as cross sections, particle emissions, etc.) is often complicated and highly energy dependent, which poses a challenge for those interested in efficiently simulating the behavior of a nuclear system. Nuclear data is released in "evaluations", which are prepared by statistically combining experimentally measured data with theoretical predictions. The most widely used format for these evaluations is called the Evaluated Nuclear Data File (ENDF) [1]. ENDF files in general are not directly used by nuclear simulations, but are pre-processed to account for simulation-specific conditions and needs such as temperature or specific data format. In Monte Carlo simulations, the ENDF file is most often converted into a more usable form, called "A Compact ENDF" (ACE) [2].

Currently, the most widely trusted code used for nuclear data pre-processing is NJOY, which has been developed and maintained at Los Alamos National Laboratory (LANL) since the early 1970's [3]. It has a large user base and is versatile for many nuclear data related tasks, including resonance reconstruction, Doppler-Broadening, multi-group cross section generation, and the preparation of thermal neutron scattering data. NJOY's capabilities are spread across 24 modules, two of which (LEAPR and THERMR) handle the calculation and representation of thermal scattering from bound moderators. The accuracy of thermal neutron scattering data can greatly dictate the quality of thermal reactor analysis and safety margin calculations, and ensuring said accuracy remains a difficult problem due to effects (molecular structure, neutron wavelength, described below) that are not apparent for higher neutron energies.

Both thermal neutron scattering and resonant neutron scattering are highly dependent on incoming neutron energy. However, thermal neutron scattering cross sections must also account for molecular structure, since the energy of the incoming neutron is generally on the order of the molecules' excitation modes (i.e. on the order of 1 eV or less). Excitation of these modes can result in vibration, translation, or rotation of the target. Vibrational modes (also called phonons, in the case of a crystal), are of primary concern

when describing neutron scattering in a solid. In addition to the molecular excitation, description of the scattering of thermal neutrons is further complicated by the neutron's long de Broglie wavelength. When a neutron has energy in the thermal region, its wavelength can be on the order of the inter-atomic spacing, which allows for the possibility for it to interact with multiple nuclei, as opposed to a single atom [4].

Despite the above complications, a thermal scattering relationship $S(\alpha, \beta, T)$ is constructed to relate unitless neutron momentum and energy exchange (α and β, respectively) with the double differential inelastic incoherent scattering cross section $\sigma\left(E \rightarrow E', \mu\right)$. Once $S(\alpha, \beta, T)$, also called the "scattering law", is obtained, the cross section can be easily calculated using

$$\sigma\left(E \rightarrow E', \mu\right) = \frac{\sigma_b}{2k_bT}\sqrt{\frac{E'}{E}}S(\alpha, \beta, T), \tag{1.1}$$

where σ_b is the characteristic bound scattering cross section of the target isotope, k_b is Boltzmann's constant, and T is the temperature. Thus, the quality of thermal nuclear system modeling is directly tied to the preparation of the scattering law.

1.2 Description of Thermal Neutron Scattering

Before further discussing LEAPR's method of calculating the scattering law $S(\alpha, \beta, T)$, it is worthwhile to introduce the various types of scattering (i.e. elastic vs. inelastic, coherent vs. incoherent), as well as describe the scattering law in terms of other commonly-discussed functions (e.g. the pair distribution function $G(\boldsymbol{r}, t)$, the intermediate scattering function $\chi(\boldsymbol{\kappa}, t)$, and the structure factor $S(\boldsymbol{\kappa}, \omega)$)[1].

1.2.1 Types of Thermal Neutron Scattering

As mentioned in Sec. 1.1, the most widely used code for nuclear data processing is NJOY, which through two of its modules (LEAPR and THERMR) has the ability to prepare thermal scattering data. Generally, LEAPR creates an $S(\alpha, \beta, T)$ table, while THERMR converts this scattering law and converts it to cross sections, then writes them to output files that are convenient to read in from simulations. Since LEAPR primarily calculates $S(\alpha, \beta, T)$, it will be of primary focus for the remainder of this section.

Thermal neutron scattering can be elastic or inelastic, both of which have a coherent and incoherent contribution. Elastic scattering implies no change in kinetic energy, while inelastic scattering does not. If the neutron elastically scatters off of a much larger target[2], the neutron itself will experience virtually no energy change, due to the scatterer's high effective mass. Inelastic thermal scattering can result in a change to neutron energy that corresponds with an excitation/de-excitation of the target.

[1] Note that for the remainder of this paper, bolded variables represent vectors.

[2] Here, "much larger target" here refers to a crystalline structure or a molecule. These examples are important to the current discussion because unlike higher energy neutrons, thermal neutrons interact with molecular structures as a whole, and not just the constituent atoms.

Excitations can correspond to creation of vibrational modes (phonons), as well as the creation of translational or rotational modes. For a system of particles with randomly distributed spins, coherent scattering consists of interacting wave effects, whereas incoherent scattering consists solely of a sum of non-interacting waves[3].

For materials with randomly distributed crystallites, the form of coherent inelastic scattering is approximately equal to that of incoherent inelastic scattering. This allows the coherent and incoherent inelastic components to be combined into one inelastic contribution, an approximation known as the "incoherent approximation", which will be further introduced in Sec. 1.2.5 [3, 5].

LEAPR separates the scattering calculation into inelastic, coherent elastic, and incoherent elastic. This project primarily focuses on inelastic scattering, due to its role in representing neutron energy change in a thermal scattering interaction.

1.2.2 Pair Distribution Function

The scattering kernel $\sigma_s(E \to E', \Omega \to \Omega')$ is typically separated into a coherent and an incoherent contribution[3], both of which can be defined in terms of so-called "van Hove pair distribution function" $G(\boldsymbol{r}, t)$, which contains information regarding the scattering material. The pair distribution function is split into two terms

$$G(\boldsymbol{r}, t) = G_s(\boldsymbol{r}, t) + G_d(\boldsymbol{r}, t) \tag{1.2}$$

which represent a "self" term and a "distinct" term, respectively. In a classical system, $G(\boldsymbol{r}, t)$ can be interpreted as the probability that an atom will be at location $\boldsymbol{r}$ at time t, given that an atom existed at the origin at time $t = 0$. The first term, $G_s(\boldsymbol{r}, t)$, represents the probability the particle originally at the origin would later exist at position $\boldsymbol{r}$. The latter term $G_d(\boldsymbol{r}, t)$ assumes that the two particles observed were not the same [7, 8].

Using these definitions of the pair distribution functions, the coherent and incoherent scattering kernels for a homogeneous system consisting of bound scatterers of a single nuclide can be described as

$$\sigma_{coh}(E \to E', \Omega \to \Omega') = \frac{\sigma_{coh}}{4\pi}\sqrt{\frac{E'}{E}}\frac{1}{2\pi}\int dt \int d\boldsymbol{r}\ \mathrm{e}^{i(\boldsymbol{\kappa}\cdot\boldsymbol{r} - \epsilon t/\hbar)} G(\boldsymbol{r}, t) \tag{1.3}$$

$$\sigma_{inc}(E \to E', \Omega \to \Omega') = \frac{\sigma_{inc}}{4\pi}\sqrt{\frac{E'}{E}}\frac{1}{2\pi}\int dt \int d\boldsymbol{r}\ \mathrm{e}^{i(\boldsymbol{\kappa}\cdot\boldsymbol{r} - \epsilon t/\hbar)} G_s(\boldsymbol{r}, t) \tag{1.4}$$

where $\hbar\boldsymbol{\kappa}$ is the change in neutron momentum, ϵ is the change in energy, and σ_{coh} and σ_{inc} are the bound coherent and incoherent scattering cross sections, respectively [8]. These bound cross sections can be defined in terms of the first and second moments of the scattering length a,

$$\sigma_{coh} = 4\pi\langle a \rangle^2 \tag{1.5}$$

[3]Note that in separating the coherent and incoherent contributions, one ignores spin-correlation effects. These effects are of little to no importance for most applications, except for instances like thermal scattering in liquid hydrogen, which has correlated spins [6]. Such materials are considered apart from this simple coherent/incoherent discussion.

$$\sigma_{inc} = 4\pi \left(\langle a^2 \rangle - \langle a \rangle^2 \right) \tag{1.6}$$

where $\langle ... \rangle$ denotes the average [9]. These definitions assume that the spins of adjacent nuclei are randomly oriented. For reactor purposes this is a very good approximation, since the spins of neighboring nuclei are typically uncorrelated except at very low temperatures.

1.2.3 Intermediate Scattering Function

The intermediate scattering function $\chi(\boldsymbol{\kappa}, t)$ serves as an intermediate step between the pair distribution function $G(\boldsymbol{r}, t)$ and the scattering law $S(\alpha, \beta)$ that we aim to describe. Note that in Eqs. 1.3, 1.4, the time-dependent term in the exponential can be moved outside the spatial integral, allowing us to define

$$\sigma_{coh}(E \to E', \Omega \to \Omega') = \frac{\sigma_{coh}}{4\pi} \sqrt{\frac{E'}{E}} \frac{1}{2\pi} \int dt \; \mathrm{e}^{-i\epsilon t/\hbar} \chi_{coh}(\boldsymbol{\kappa}, t) \tag{1.7}$$

$$\sigma_{inc}(E \to E', \Omega \to \Omega') = \frac{\sigma_{inc}}{4\pi} \sqrt{\frac{E'}{E}} \frac{1}{2\pi} \int dt \; \mathrm{e}^{-i\epsilon t/\hbar} \chi_{inc}(\boldsymbol{\kappa}, t) \tag{1.8}$$

where

$$\chi_{coh}(\boldsymbol{\kappa}, t) = \int \mathrm{e}^{i\boldsymbol{\kappa}\cdot\boldsymbol{r}} G(\boldsymbol{r}, t) \; d\boldsymbol{r} \tag{1.9}$$

$$\chi_{inc}(\boldsymbol{\kappa}, t) = \int \mathrm{e}^{i\boldsymbol{\kappa}\cdot\boldsymbol{r}} G_s(\boldsymbol{r}, t) \; d\boldsymbol{r}. \tag{1.10}$$

1.2.4 Structure Factor

The structure factor $S(\boldsymbol{\kappa}, \epsilon)$ is the space and time Fourier transform of the correlation function $G(\boldsymbol{r}, t)$ (i.e. the time Fourier transform of the intermediate scattering function $\chi(\boldsymbol{\kappa}, t)$),

$$S(\boldsymbol{\kappa}, \epsilon) = \frac{1}{2\pi} \int_{-\infty}^{\infty} \int \mathrm{e}^{i(\boldsymbol{\kappa}\cdot\boldsymbol{r} - \epsilon t/\hbar)} \; G(\boldsymbol{r}, t) \; d\boldsymbol{r} \; dt \tag{1.11}$$

$$S_s(\boldsymbol{\kappa}, \epsilon) = \frac{1}{2\pi} \int_{-\infty}^{\infty} \int \mathrm{e}^{i(\boldsymbol{\kappa}\cdot\boldsymbol{r} - \epsilon t/\hbar)} \; G_s(\boldsymbol{r}, t) \; d\boldsymbol{r} \; dt. \tag{1.12}$$

By applying the principle of detailed balance[4] to Eqs. 1.11, 1.12, we find that the structure factor is seen to be symmetric [8]. Recalling that

$$\hbar^2 \kappa^2 = |m\boldsymbol{v} - \boldsymbol{v}'|^2 \tag{1.13}$$

$$= m(v)^2 + m(v')^2 - 2\mu v v' \tag{1.14}$$

$$= 2E + 2E' - 4\mu\sqrt{EE'}, \tag{1.15}$$

[4]Detailed balance asserts that for a system at thermodynamic equilibrium, any microscopic processes must be equilibrated by the corresponding reverse process. For this discussion on scattering, detailed balance requires that the rate at which neutrons that scatter out of energy E must equal the rate at which neutrons scatter into energy E (assuming thermal equilibrium).

the dimensionless version of which is defined as

$$\alpha = \frac{\hbar^2\kappa^2}{2Amk_bT} = \frac{E' + E - 2\mu\sqrt{EE'}}{Ak_bT} \tag{1.16}$$

where μ is the cosine of the scattering angle in the lab frame (all azimuthal angles are considered equally likely), A is the target mass number, and k_bT is the scatterer temperature in energy (k_b is the Boltzmann constant). Similarly, the dimensionless energy transfer is defined as

$$\beta = -\frac{\epsilon}{k_bT} = \frac{E' - E}{k_bT}. \tag{1.17}$$

Using these dimensionless versions of $\boldsymbol{\kappa}$ and ϵ, the structure factor $S(\boldsymbol{\kappa}, \epsilon)$ can be rewritten as

$$S_{sym}(\alpha, \beta) = k_bT\mathrm{e}^{\beta/2}\ S(\boldsymbol{\kappa}, \epsilon) \tag{1.18}$$

where the "sym" subscript indicates that the symmetric nature of the structure factor has carried over to the scattering law. Note that for the duration of this paper, the non-symmetric form of the scattering law will be of primary interest, and will be further discussed in Sec. 1.3.1.

$$\sigma_{coh}(E \to E', \Omega \to \Omega') = \frac{\sigma_{coh}}{4\pi}\sqrt{\frac{E'}{E}}\frac{1}{2\pi}\int dt \int d\boldsymbol{r}\ \mathrm{e}^{i(\boldsymbol{\kappa}\cdot\boldsymbol{r} - \epsilon t/\hbar)}G(\boldsymbol{r}, t) \tag{1.19}$$

$$= \frac{\sigma_{coh}}{4\pi}\sqrt{\frac{E'}{E}}S(\boldsymbol{\kappa}, \epsilon) \tag{1.20}$$

$$= \frac{\sigma_{coh}}{4\pi k_bT}\sqrt{\frac{E'}{E}}S_{sym}(\alpha, \beta)\mathrm{e}^{-\beta/2}. \tag{1.21}$$

$$\tag{1.22}$$

By assuming that scattering is isotropic in the azimuthal direction, we can integrate across the azimuthal angle and make this cross section instead a function of the scattering cosine μ,

$$\sigma_{coh}(E \to E', \mu) = \frac{\sigma_{coh}}{2k_bT}\sqrt{\frac{E'}{E}}S_{sym}(\alpha, \beta)\mathrm{e}^{-\beta/2}. \tag{1.23}$$

1.2.5 Incoherent Approximation

As mentioned in Sec. 1.2.2, the total scattering cross section has both a coherent and an incoherent contribution. The coherent component is defined using a bound coherent scattering cross section σ_{coh}, along with a scattering law related to the full pair correlation function $G(\boldsymbol{r}, t)$. Similarly, the incoherent scattering cross section is defined using a bound incoherent scattering cross section σ_{inc} and a scattering law related to the "self" pair correlation function $G_s(\boldsymbol{r}, t)$.

Often, the "incoherent approximation" is applied, which simply assumes that $G(\boldsymbol{r},t) \approx G_s(\boldsymbol{r},t)$, meaning that the total scattering cross section is defined as

$$\sigma(E \to E',\mu) = \frac{\sigma_{coh}+\sigma_{inc}}{2}\sqrt{\frac{E'}{E}}\frac{1}{2\pi}\int dt \int d\boldsymbol{r}\ \mathrm{e}^{i(\boldsymbol{\kappa}\cdot\boldsymbol{r}-\epsilon t/\hbar)}G_s(\boldsymbol{r},t). \tag{1.24}$$

In terms of the scattering law, this approximation allows the cross section to be written as

$$\sigma(E \to E',\mu) = \frac{\sigma_{coh}+\sigma_{inc}}{2k_bT}\mathrm{e}^{-\beta/2}\sqrt{\frac{E'}{E}}S_{sym}(\alpha,\beta). \tag{1.25}$$

For a brief discussion on the validity of this approximation, specifically regarding hydrogenous materials, see Appendix A.1.

1.3 Current Methods of Preparing $S(\alpha,\beta,T)$

With a general picture of what the scattering law $S(\alpha,\beta)$ means and where it comes from, we can begin to explore how it is typically calculated (following the methodology used in NJOY's LEAPR module [3]).

1.3.1 Inelastic Thermal Neutron Scattering

Recall from Sec. 1.1 that the double differential inelastic cross section for a given temperature T is defined as

$$\sigma\left(E \to E',\mu\right) = \frac{\sigma_b}{2k_bT}\sqrt{\frac{E'}{E}}S_{n.sym}(\alpha,\beta,T) \tag{1.1}$$

which describes a neutron with incoming energy E scattering with cosine μ into energy E', where σ_b is the target's characteristic bound scattering cross section, and k_b is Boltzmann's constant. Note that $S_{n.sym}(\alpha,\beta,T)$ is the non-symmetric form of the scattering law, which is related to the symmetric form by

$$S_{sym}(\alpha,\beta,T) = \mathrm{e}^{\beta/2}S_{n.sym}(\alpha,\beta,T). \tag{1.26}$$

Recall that dimensionless momentum and energy transfer, α and β respectively, between a neutron and a target of mass number A, are defined as

$$\alpha = \frac{E'+E-2\mu\sqrt{E'E}}{Ak_bT} \tag{1.16}$$

$$\beta = \frac{E'-E}{k_bT}. \tag{1.17}$$

The minimum value that β can have occurs when $E'=0$, meaning that $\beta = -E/k_bT$. β can be arbitrarily high, but is often cutoff to some reasonably high value (e.g. $\beta_{\max} = 20.0$

in [10]). For a each β value, there exists a valid range of α values, which will be further discussed in Sec. 1.2.

The non-symmetric scattering law $S_{n.sym}(\alpha, \beta)$ can be written as an integral across unitless time[5],

$$S_{n.sym}(\alpha, \beta, T) = \frac{1}{2\pi} \int_{-\infty}^{\infty} e^{i\beta\hat{t}} e^{-\gamma(\hat{t})} \, d\hat{t} \tag{1.27}$$

where [3]

$$\gamma(\hat{t}) = \alpha \int_{-\infty}^{\infty} P(\beta) \left[1 - e^{-i\beta\hat{t}}\right] e^{-\beta/2} \, d\beta \tag{1.28}$$

and

$$P(\beta) = \frac{\rho(\beta)}{2\beta \sinh(\beta/2)}. \tag{1.29}$$

Here, $\rho(\beta)$ is the frequency spectrum (also called the "vibrational density of states" or "phonon distribution" for a crystal) that is characteristic to the material, such that $\rho(\beta)\, d\beta$ describes the probability that the lattice will experience normal modes of vibration between β and $\beta + d\beta$ [8]. The frequency spectrum normalizes to unity,

$$\int_0^{\infty} \rho(\beta) d\beta = 1. \tag{1.30}$$

Eq. 1.27 uses the Gaussian approximation[6], as well as the incoherent approximation, which neglects interference effects [11]. The forms of Eqs. 1.27, 1.28 were obtained assuming that the scattering material has a simple cubic crystal structure [8]. Further assumptions include that there exists only one type of atom, and that atoms are bound by harmonic interatomic forces in a structure with cubic symmetry. Despite these restrictive assumptions, Eqs. 1.27, 1.28 tend to return relatively accurate inelastic cross sections for many materials that do not adhere to the aforementioned assumptions (e.g. materials that lack cubic structure) [8].

To facilitate the calculation of Eq. 1.27, LEAPR decomposes the frequency spectrum $\rho(\beta)$,

$$\rho(\beta) = \sum_{j=1}^{\#\text{ osc.}} \omega_j \delta(\beta - \beta_j) + \rho_s(\beta) + \rho_t(\beta) \tag{1.31}$$

into a sum of discrete oscillators (represented by weighted delta-functions $\omega_j \delta(\beta - \beta_j)$), a solid-type spectrum $\rho_s(\beta)$, and a translational spectrum $\rho_t(\beta)$. The solid-type spectrum

[5]Note that this "time" parameter is related to the time t that was used in Sec. 1.2.2-1.2.5. The values defined in preceding sections, ϵ and t, are replaced with corresponding unitless values, β and $\hat{t}$. If $\beta\hat{t} = \epsilon t/\hbar$ where $\beta = k_b T\epsilon$, then $\hat{t} = t\ k_b T/\hbar$.

[6]In general, the intermediate scattering function is such that $\ln(\chi_{inc}(\kappa, t)) = -\kappa^2\gamma(t) + \kappa^4\gamma_2(t) + \ldots$ where $\ln(\chi_{inc}(\kappa, t)) \approx -\kappa^2\gamma(t)$ corresponds to the Gaussian approximation. This approximation is exact for systems such as the isotropic Einstein oscillator with harmonic lattice vibrations, and is relatively valid for anisotropic vibrations as long as κ^2 is small [6]. The remainder of this project assumes the Gaussian approximation to be valid for all cases considered.

and translational spectrum integrate to ω_s and ω_t, respectively, such that

$$\sum_{j=1}^{\#\text{ osc.}} \omega_j + \omega_s + \omega_t = 1. \tag{1.32}$$

LEAPR uses each component of this decomposed frequency distribution to create a corresponding scattering law, then convolves these individual scattering laws to retrieve the true scattering relation $S_{n.sym}(\alpha, \beta, T)$.

Solid-Type Continuous Spectra

The solid-type continuous contribution, denoted as $S^{(s)}_{n.sym}(\alpha, \beta, T)$, can be simplified by representing Eq. 1.27 as an infinite sum, and using a finite number of terms of that sum to approximate a contribution value. The solid-type continuous spectra depends on the frequency distribution $\rho(\beta)$. Eq. 1.28 can be rewritten as

$$\gamma(\hat{t}) = \alpha\lambda_s - \alpha \int_{-\infty}^{\infty} P(\beta) \mathrm{e}^{-\beta/2} \mathrm{e}^{-i\beta\hat{t}}\, d\beta, \tag{1.33}$$

where λ_s, known as the Debye-Waller coefficient for the solid-type spectra, is defined as

$$\lambda_s = \int_{-\infty}^{\infty} P(\beta') \mathrm{e}^{-\beta'/2}\, d\beta' \tag{1.34}$$

The exponential of $\gamma(\hat{t})$ is approximated as

$$\mathrm{e}^{-\gamma(\hat{t})} = \sum_{n=0}^{\infty} \left(\mathrm{e}^{-\alpha\lambda_s} \frac{1}{n!} \left[\alpha \int_{-\infty}^{\infty} P(\beta') \mathrm{e}^{-\beta'/2} \mathrm{e}^{-i\beta'\hat{t}}\, d\beta' \right]^n \right) \tag{1.35}$$

where the exponential of Eq. 1.33's latter term has been represented using a Taylor series. Eq. 1.35 is used in Eq. 1.27 to yield [3, 8]

$$S^{(s)}_{n.sym}(\alpha, \beta, T) = \frac{1}{2\pi} \int_{-\infty}^{\infty} \mathrm{e}^{i\beta\hat{t}} \sum_{n=0}^{\infty} \left(\mathrm{e}^{-\alpha\lambda_s} \frac{1}{n!} \left[\alpha \int_{-\infty}^{\infty} P(\beta') \mathrm{e}^{-\beta'/2} \mathrm{e}^{-i\beta'\hat{t}}\, d\beta' \right]^n \right) d\hat{t} \tag{1.36}$$

$$= \mathrm{e}^{-\alpha\lambda_s} \sum_{n=0}^{\infty} \frac{\alpha^n}{n!} \frac{1}{2\pi} \int_{-\infty}^{\infty} \mathrm{e}^{i\beta\hat{t}} \left[\int_{-\infty}^{\infty} P(\beta') \mathrm{e}^{-\beta'/2} \mathrm{e}^{-i\beta'\hat{t}}\, d\beta' \right]^n d\hat{t} \tag{1.37}$$

$$= \mathrm{e}^{-\alpha\lambda_s} \sum_{n=0}^{\infty} \frac{1}{n!} [\alpha\lambda_s]^n \mathcal{T}_n(\beta) \tag{1.38}$$

where

$$\lambda_s^n \mathcal{T}_n(\beta) = \frac{1}{2\pi} \int_{-\infty}^{\infty} \mathrm{e}^{i\beta\hat{t}} \left[\int_{-\infty}^{\infty} P(\beta') \mathrm{e}^{-\beta'/2} \mathrm{e}^{-i\beta'\hat{t}}\, d\beta' \right]^n d\hat{t}\,. \tag{1.39}$$

This definition of the scattering law is referred to as the "phonon expansion", since the n^{th} term corresponds to the excitation of n modes in the scatterer (i.e. creation of n phonons in the material) [8].

Note that

$$\mathcal{T}_0(\beta) = \delta(\beta) \tag{1.40}$$

and

$$\mathcal{T}_1(\beta) = \frac{1}{2\pi\lambda_s}\int_{-\infty}^{\infty} \mathrm{e}^{i\beta\hat{t}} \int_{-\infty}^{\infty} P(\beta')\mathrm{e}^{-\beta'/2}\mathrm{e}^{-i\beta'\hat{t}}\, d\beta'\, d\hat{t} \tag{1.41}$$

$$= \frac{1}{2\pi\lambda_s}\int_{-\infty}^{\infty} P(\beta')\mathrm{e}^{-\beta'/2} \int_{-\infty}^{\infty} \mathrm{e}^{i(\beta-\beta')\hat{t}}\, d\hat{t}\, d\beta' \tag{1.42}$$

$$= \frac{1}{\lambda_s}\int_{-\infty}^{\infty} P(\beta')\mathrm{e}^{-\beta'/2}\delta(\beta-\beta')\, d\beta' \tag{1.43}$$

$$= \frac{P(\beta)\mathrm{e}^{-\beta/2}}{\lambda_s}. \tag{1.44}$$

As shown in Appendix A.2, $\mathcal{T}_n(\beta)$ can be attained by convolving the previous function $T_{n-1}(\beta)$ with $T_1(\beta)$,

$$\mathcal{T}_n(\beta) = \int_{-\infty}^{\infty} \mathcal{T}_1(\beta')\, \mathcal{T}_{n-1}(\beta-\beta')\, d\beta'. \tag{1.45}$$

Approximating the solid-type, continuous contribution to $S_{n.sym}(\alpha,\beta,T)$ can be done by computing $\mathcal{T}_i(\beta)$ for i from 1 to a sufficiently large value of n. These $\mathcal{T}_i(\beta)$ values are then provided to the sum in Eq. 1.38.

Discrete Oscillator

The phonon distribution for H in H_2O according to the CAB model [12], which is based off of experimental measurements and molecular dynamics simulations, is shown in Fig. 1.1. Often, vibrational modes appear as sharp peaks in the frequency distribution, which are commonly approximated in LEAPR as weighted Dirac-δ functions, $\rho(\beta) = \omega_i\delta_i(\beta-\beta_i)$. The contribution to the scattering law from oscillator i is

$$S^{(i)}_{n.sym}(\alpha,\beta) = \mathrm{e}^{-\alpha\lambda_i}\sum_{n=-\infty}^{\infty}\delta(\beta-n\beta_i)\,\mathrm{I}_n\left[\frac{\alpha w_i}{\beta_i\sinh(\beta_i/2)}\right]\mathrm{e}^{-n\beta_i/2} \tag{1.46}$$

where the corresponding Debye-Waller coefficient is

$$\lambda_i = w_i\frac{\coth(\beta_i/2)}{\beta_i} \tag{1.47}$$

and $\mathrm{I}_n(x)$ is the modified Bessel function of the first kind. Note that while Eqs. 1.46, 1.47 seem to differ significantly from their continuous-spectrum counterparts, they are actually equivalent to the solid type scattering law contribution, with the only additional assumption being that $\rho(\beta) = \omega_i\ \delta(\beta-\beta_i)$, as shown in Appendix C.2.

When combining a continuous, solid-type spectrum with N discrete oscillators, the total Debye-Waller coefficient is simply the sum of each contributions' Debye-Waller coefficient,

$$\lambda = \lambda_s + \sum_{i=1}^{N}\lambda_i. \tag{1.48}$$

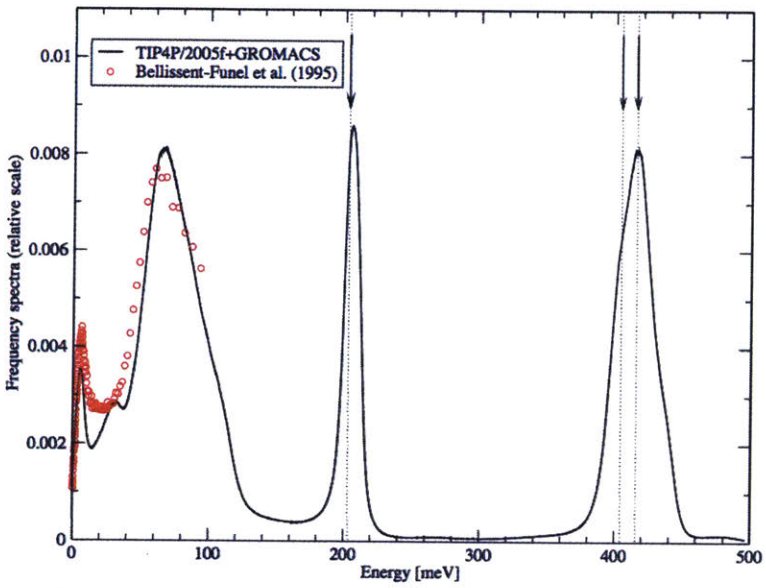

Figure 1.1: Phonon distribution for H in H_2O [12]. The red points and the arrows represent measured data against which to compare the calculated spectrum. Of particular interest are the two peaks near 200 and 400 meV, which in typical NJOY LEAPR inputs are approximated as discrete oscillators.

By collecting the Bessel function and exponentials in Eq. 1.46, the discrete oscillator contribution to the scattering law can be rewritten as

$$S^{(i)}_{n.sym}(\alpha,\beta) = \sum_{n=-\infty}^{\infty} A_{i,n}(\alpha)\delta\left(\beta - n\beta_i\right) \tag{1.49}$$

where $A_{i,n}(\alpha)$ is defined as

$$A_{i,n}(\alpha) = \mathrm{e}^{-\alpha\lambda_i}\mathrm{I}_n\left[\frac{\alpha\omega_i}{\beta_i \sinh(\beta_i/2)}\right]\mathrm{e}^{-n\beta_i/2}. \tag{1.50}$$

Using Eq. 1.49, the contribution that an individual oscillator has to the total scattering law is rather simple to compute. However, once computed, it must be convolved with the other contribution(s) to the scattering law. To illustrate this process, consider an example where two discrete oscillators contributions, $S^{(1)}_{n.sym}$ and $S^{(2)}_{n.sym}$, are combined with a solid-type contribution $S^{(s)}_{n.sym}$. To begin, the first oscillator is combined with the

solid-type spectrum,

$$S^{(s,1)}_{n.sym}(\alpha,\beta) = \int_{-\infty}^{\infty} S^{(1)}_{n.sym}(\alpha,\beta')\, S^{(s)}_{n.sym}(\alpha,\beta-\beta')\, d\beta' \tag{1.51}$$

$$= \int_{-\infty}^{\infty} \sum_{n=-\infty}^{\infty} A_{1,n}(\alpha)\delta(\beta'-\beta_1)\, S^{(s)}_{n.sym}(\alpha,\beta-n\beta')\, d\beta' \tag{1.52}$$

$$= \sum_{n=-\infty}^{\infty} A_{1,n}(\alpha) S^{(s)}_{n.sym}(\alpha,\beta-n\beta_1) \tag{1.53}$$

and the second oscillator can then be combined to the other two contributions,

$$S^{(s,1,2)}_{n.sym}(\alpha,\beta) = \int_{-\infty}^{\infty} S^{(2)}_{n.sym}(\alpha,\beta')\, S^{(s,1)}_{n.sym}(\alpha,\beta-\beta')\, d\beta' \tag{1.54}$$

$$= \int_{-\infty}^{\infty} \sum_{m=-\infty}^{\infty} A_{2,m}(\alpha)\delta(\beta'-m\beta_2)\, S^{(s,1)}_{n.sym}(\alpha,\beta-\beta')\, d\beta' \tag{1.55}$$

$$= \sum_{m=-\infty}^{\infty} A_{2,m}(\alpha) S^{(s,1)}_{n.sym}(\alpha,\beta-m\beta_2) \tag{1.56}$$

$$= \sum_{m=-\infty}^{\infty} A_{2,m}(\alpha) \sum_{n=-\infty}^{\infty} A_{1,n}(\alpha) S^{(s)}_{n.sym}(\alpha,\beta-n\beta_1-m\beta_2) \tag{1.57}$$

Depending on the size of the α,β grids, and the number of δ functions considered, convolving the oscillator contributions with the continuous, solid-type spectrum can be a tedious calculation, and will be further discussed in Sec. 2.

Translational Spectra

For some materials (e.g. gases, liquids), thermal neutron scattering can be modeled by combining a diffusive term $S^{(t)}_{n.sym}$ to a solid-type continuous contribution. Two options exist for this translational/diffusive term: the "effective width model" and the "free gas model", which are generally used for liquid moderators and gaseous moderators, respectively [13, 3]. Both formulations allow for analytic expressions of the scattering law which, once calculated, is convolved with other contributions to obtain the total $S_{n.sym}(\alpha,\beta)$.

1.3.2 Compatible α,β Values

Recalling the definitions of α and β that were introduced in Eqs. 1.16-1.17, respectively, it is apparent that not all (α,β) pairs are physically compatible. For a given β value, the minimum α value corresponds to no change in angle ($\mu = 1$), and the maximum α value corresponds to back scattering ($\mu = -1$). Thus, setting $\mu = \pm 1$ gives the minimum and maximum α values, respectively,

$$\alpha_{min,max} = \frac{E' + E \mp 2\sqrt{E'E}}{Ak_bT}. \tag{1.58}$$

Using the definition of β in Eq. 1.17 to eliminate E', the bounding α values are represented as

$$\alpha_{min,max} = \frac{(\beta k_b T + E) + E \mp 2\sqrt{(\beta k_b T + E)E}}{A k_b T} \tag{1.59}$$

$$= \frac{\left(\sqrt{\beta k_b T + E} \mp \sqrt{E}\right)^2}{A k_b T}. \tag{1.60}$$

Thus for a given β, temperature T, initial neutron energy E, and mass ratio A, the valid α range is

$$\frac{\left(\sqrt{\beta k_b T + E} - \sqrt{E}\right)^2}{A k_b T} \leq \alpha \leq \frac{\left(\sqrt{\beta k_b T + E} + \sqrt{E}\right)^2}{A k_b T}. \tag{1.61}$$

This relationship in Eq. 1.61 is plotted in Fig. 1.2, where a neutron with initial energy $E = 0.0255$ eV scatters off of H in H_2O at $T = 296$ K. In all subsequent discussions,

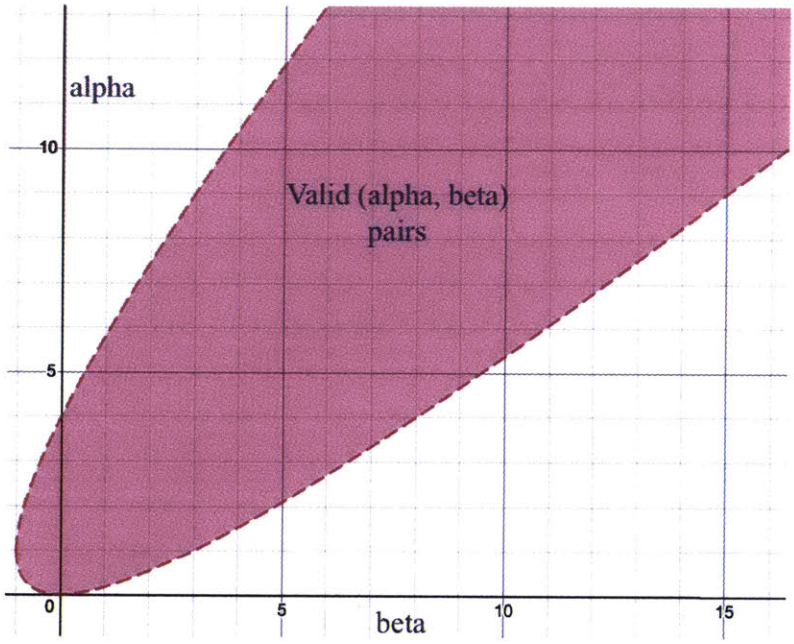

Figure 1.2: Valid (α, β) combinations, given a 0.0255 eV neutron scattering from H in H_2O. This illustrates the requirement presented in Eq. 1.61.

only α and β values that satisfy the requirement in Eq. 1.61 for the given temperature, initial energy, and mass number, will be presented, so as to restrict the conclusions to only include physically meaningful values.

1.4 Current Methods of Sampling from $S(\alpha, \beta, T)$

Computing the scattering law, as described in Sec. 1.3, requires making many choices regarding approximations and assumptions about the moderator. Once the scattering law is obtained, further care is required to enable efficient and accurate sampling. Since $S(\alpha, \beta, T)$ requires sufficiently fine α, β grids, in addition to having a temperature dependence, there exists the risk of prohibitively large memory usage. To combat this potential restriction, a fitting approach in temperature has been introduced, which uses probability distributions to facilitate sampling α and β values for the simulation [10]. This fitting approach will be introduced in Sec. 1.4.2. First, however, a quick introduction to how the cross section values are written to the ENDF-style output is provided.

1.4.1 Generation of Pointwise ENDF

Recall Eq. 1.1, which shows that once the scattering law is obtained, the incoherent scattering cross section can be easily calculated,

$$\sigma^{\text{inc.}}(E \to E', \mu, T) = \frac{\sigma_b}{2k_bT}\sqrt{\frac{E'}{E}}S_{n.sym}(\alpha, \beta, T). \tag{1.1}$$

Generally, the LEAPR module of NJOY prepares the scattering law $S_{n.sym}(\alpha, \beta, T)$ and provides it to THERMR, which then generates pointwise cross sections and $E \to E'$ scattering matrices for every desired temperature T. This act of reproducing tables for each temperatures is what prompted the development of the sampling technique that will be described in Sec. 1.4.2. THERMR writes the scattering data to a pointwise-ENDF (PENDF), which can later be used by other modules for further processing and/or plotting. When the cross sections are written to the PENDF file, two possible orderings are allowed: E-E'-μ and E-μ-E'. The former is significantly more popular, while the latter is primarily used for comparing against experiments.

Thermal neutron scattering data is prepared by the LEAPR and THERMR modules of NJOY, where LEAPR typically uses a frequency distribution to generate the scattering law and THERMR produces point-wise scattering cross sections [3].

Inelastic scattering cross sections, outgoing energies, and equiprobable angles are typically provided to nuclear calculations. If a neutron initially has energy E, the interpolation factor f is defined as

$$f = \frac{E - E_i}{E_{i+1} - E_i} \tag{1.62}$$

where the E lies between E_i and E_{i+1} [14]. This interpolation factor is used to sample outgoing energy E',

$$E' = E_{i,j} + f\Big(E_{i+1,j} - E_{i,j}\Big). \tag{1.63}$$

Incoming and outgoing energy bins are represented with i and j, respectively. The outgoing scattering cosines are sampled are sampled in a similar way

$$\mu = \mu_{i,j,k} + f\Big(\mu_{i+1,j,k} - \mu_{i,j,k}\Big) \tag{1.64}$$

where k designates the scattering cosine bins [14].

1.4.2 Generation of $S(\alpha, \beta, T)$ Probability Distribution

Joint Probability Distribution

To avoid prohibitively large memory usage and provide a rigorous continuous energy and angle representation, a fitting approach in α and β space [15] as well as a fitting approach in temperature [10] have been developed, so as to ease the burden of storing vast amounts of data. The fitting approach in temperature is of primary focus here, and requires construction of the scattering cross sections' probability density functions (PDF) and cumulative distribution functions (CDF), as functions of α and β. The cross section $\sigma^{inc}(E \rightarrow E', \mu, T)$ defined in Eq. 1.1 is converted to α and β dependence,

$$\sigma^{\text{inc.}}(\alpha, \beta, T) = \frac{Ak_bT\sigma_b}{4E} S_{n.sym}(\alpha, \beta, T). \tag{1.65}$$

Once Eq. 1.65 is normalized to integrate to 1, it is interpreted as a joint probability distribution,

$$f(\alpha, \beta | E, T) = \frac{\sigma^{\text{inc.}}(\alpha, \beta, T)}{\int_{\beta_{\min}}^{\beta_{\max}} \int_{\alpha_{\min}}^{\alpha_{\max}} \sigma^{\text{inc.}}(\alpha', \beta', T) d\alpha' \, d\beta'} \tag{1.66}$$

where initial neutron energy E is held fixed. Constant factors cancel out, leaving

$$f(\alpha, \beta | E, T) = \frac{S_{n.sym}(\alpha, \beta, T)}{\int_{\beta_{\min}}^{\beta_{\min}} \int_{\alpha_{\min}}^{\alpha_{\min}} S_{n.sym}(\alpha', \beta', T) d\alpha' \, d\beta'}. \tag{1.67}$$

Minimum and Maximum α, β Values

As stated in Eq. 1.61, the bounding α range, for given values of β, T, and A, is defined by

$$\frac{\left(\sqrt{\beta k_b T + E} - \sqrt{E}\right)^2}{Ak_bT} \leq \alpha \leq \frac{\left(\sqrt{\beta k_b T + E} + \sqrt{E}\right)^2}{Ak_bT}. \tag{1.61}$$

These bounding α values serve as the integration bounds $\alpha_{\min}, \alpha_{\max}$ in Eq. 1.67, and are a function of incoming energy E and β'. The minimum β value occurs when $E' = 0$, leaving a $\beta_{\min} = -E/k_bT$. The maximum β value, however, is less well-defined, since theoretically a neutron can be up-scattered to an arbitrarily high energy. But for the purposes of this discussion, the convention used by [10] is adopted, and the maximum energy transfer is set to a reasonably high value $\beta_{\max} = 20$.

Probability Distribution Functions

Following the notation in [10], two conditional probability distributions are constructed (PDF in β given E, and PDF of α given β). The former is obtained by integrating

Eq. 1.67 across α',

$$g(\beta|E,T) = \frac{\int_{\alpha_{\min}}^{\alpha_{\max}} S_{n.sym}(\alpha',\beta,T)\, d\alpha'}{\int_{\beta_{\min}}^{\beta_{\max}} \int_{\alpha_{\min}}^{\alpha_{\max}} S_{n.sym}(\alpha',\beta',T) d\alpha'\, d\beta'}. \tag{1.68}$$

where the latter is obtained by removing the integration across β' from Eq. 1.67,

$$h(\alpha|\beta,E,T) = \frac{S_{n.sym}(\alpha,\beta,T)}{\int_{\alpha_{\min}}^{\alpha_{\max}} S_{n.sym}(\alpha',\beta,T) d\alpha'}. \tag{1.69}$$

The PDFs, $g(\beta|E,T)$ and $h(\alpha|\beta,E,T)$, can be integrated to obtain their respective CDFs, $G(\beta|E,T)$ and $H(\alpha|\beta,E,T)$,

$$G(\beta|E,T) = \int_{\beta_{\min}}^{\beta} g\left(\beta'|E,T\right) d\beta' \tag{1.70}$$

$$H(\alpha|\beta,E,T) = \int_{\alpha_{\min}}^{\alpha} h\left(\alpha'|\beta,E,T\right) d\alpha'. \tag{1.71}$$

Note that Eq. 1.71 has dependence on β, E, and T, meaning that storing the CDF for α given β would be quite costly. The dependence on incoming neutron energy E can be eliminated, however, by refusing to account for the α bounds (which are the only terms with E dependence). This of course will result in non-physical (α, β) pairs (i.e. they will not comply with Eq. 1.61), but such conflicts can be readily resolved. Eqs. 1.69 and 1.71 are rewritten to be energy independent,

$$\hat{h}(\alpha|\beta,T) = \frac{S(\alpha,\beta,T)}{\int_0^{\alpha_\infty} S(\alpha',\beta,T) d\alpha'} \tag{1.72}$$

$$\hat{H}(\alpha|\beta,T) = \int_0^{\alpha} \hat{h}\left(\alpha'|\beta,T\right) d\alpha'. \tag{1.73}$$

As seen in Sec. B.2, Eq. 1.73 can be amended so that the $\hat{H}$ CDF values with non-physical α, β values are removed [10],used to enforce the α restrictions that were dropped when removing incoming neutron energy dependence [10],

$$H(\alpha|\beta,E,T) = \frac{\hat{H}(\alpha|\beta,T) - \hat{H}(\alpha_{\min}|\beta,T)}{\hat{H}(\alpha_{\max}|\beta,T) - \hat{H}(\alpha_{\min}|\beta,T)}. \tag{1.74}$$

Thus, during the preprocessing step, $\hat{H}(\alpha|\beta,T)$ and $G(\beta|E,T)$ are calculated and stored. Due to its relative simplicity, $G(\beta|E,T)$ can be directly sampled. Using the resulting β value from $G(\beta|E,T)$, $\hat{H}(\alpha|\beta,T)$ is sampled and Eq. 1.74 is used to remove non-physical (α, β) combinations, which eliminates the need to tabulate the α CDF against incoming neutron energy E.

1.4.3 Sampling from $S(\alpha, \beta, T)$ Probability Distribution

In this section, the method for sampling α, β values is presented, by using the CDFs that were constructed in Sec. 1.4.2, where the initial neutron energy E and the temperature of the material T are known.

1. β value is sampled [10]
   (a) The β range is set to be $[-E/k_bT, 20 \text{ eV}]$.
   (b) For each β value, its corresponding $\alpha_{\min}, \alpha_{\max}$ values are calculated using Eq. 1.61.
   (c) These α values are then used to construct the β PDF $g(\beta|E,T)$ as well as the β CDF $G(\beta|E,T)$ defined in Eqs. 1.68,1.70.
   (d) A pseudo-random number ξ_1 is sampled between [0,1], and is equated to the CDF $G(\beta|E,T)$.
   (e) A search of the CDF table is performed to locate the value of β such that $G(\beta|E,T) = \xi_1$.
2. α value is sampled [10]
   (a) For the β value that was just sampled, calculate its $\alpha_{\min}$ and $\alpha_{\max}$.
   (b) The α CDF $\hat{H}(\alpha|\beta,T)$ is calculated from Eq. 1.73.
   (c) $\hat{H}(\alpha_{\min}|\beta,T)$ and $\hat{H}(\alpha_{\max}|\beta,T)$ are calculated.
   (d) A pseudo-random number ξ_2 is sampled between [0,1], and is equated to the α CDF $H(\alpha|\beta,E,T)$.
   (e) With $\xi_2 = H(\alpha|\beta,E,T)$, Eq. 1.73 is used to solve for $\hat{H}(\alpha|\beta,T)$.

$$\hat{H}(\alpha|\beta,T) = \xi_2 \left[\hat{H}\left(\alpha_{\max}|\beta,T\right) - \hat{H}\left(\alpha_{\min}|\beta,T\right)\right] + \hat{H}\left(\alpha_{\min}|\beta,T\right) = \xi_3 \quad (1.75)$$

   (f) A search on the CDF $\hat{H}(\alpha|\beta,T)$ table is performed to find some α such that Eq. 1.75 is valid.

Chapter 2

Thesis Objectives

The process of preparing thermal neutron scattering data for simulations involves a number of outdated methods and approximations, that were introduced in Sec. 1.3. This section is dedicated to further identifying specific inadequacies in current thermal data processing methods. Some of these inadequacies are simple to fix (e.g. checking for convergence instead of setting fixed summation limits). However, others are more foundational, and thus require discussion and potentially removal from the nuclear data processing code (e.g. the approximation made in Eq. 1.31 which separates the frequency spectrum into a set of discrete oscillators, a solid-type contribution, and a diffusive term). Perhaps the most severe limitation currently employed in the NJOY LEAPR code is the restriction of the input phonon distribution to be on a uniform grid (this will be further discussed in Sec. 2.2.1).

The objectives of this project are to

1. Provide analysis into the effects of the discrete oscillator approximation
2. Discuss specific instances where calculation methods are deprecated
3. Motivate and discuss the development of a nonuniform phonon distribution energy grid
4. Implement the PDF/CDF sampling method developed by [10] into the OpenMC Python API [16].

2.1 Input Phonon Distribution Approximations

When the frequency distribution is decomposed in Eq. 1.31, it is broken into a solid-type continuous part, translational/diffusive part, and a series of discrete oscillators. The solid-type, continuous representation involved directly solving Eq. 1.45. The translational/diffusive part is approximated by either convolving a diffusive term to the existing solid-type spectrum, or by using a free-gas approximation. The discrete oscillators rep-

resent vibrational modes in polyatomic molecules, and are approximated as δ functions in the phonon distribution [3].

The choice to approximate vibrational modes as discrete oscillators was made as an attempt to reduce the computational toll that may otherwise exist. Approximating a peak in the frequency distribution as an oscillator allows for analytic forms of both $S^{(i)}(n.sym)(\alpha,\beta,T)$ and the phonon distribution $\rho(\beta)$. This benefit is counteracted, however, by the need to convolve the separately calculated scattering laws (one for solid-type continuous, and perhaps one for translational/diffusive, and perhaps one or more for discrete oscillator), as is demonstrated in Eq. 1.51-1.57.

Furthermore, in order to use LEAPR's discrete oscillator approximation, the user must either create or otherwise obtain a partial phonon spectrum, which omits key peaks (since those peaks will be represented using δ functions). The user would place a δ function at the center of each peak, and must define the δ function's corresponding weight such that it adequately represents the area under the original peak. In practice, this results in users simply copying and pasting existing input files from one source to the next, since generating a file from scratch requires so much additional effort. This dependency on pre-existing input files makes LEAPR less accessible to users who need to process thermal scattering data for materials other than those typically documented[1] and less adaptable to more accurate phonon distributions.

Since the discrete oscillator approximation (1) is not conducive to newer materials and incentivizes relying on decades-old input files, and (2) negates some of its appeal by requiring convolution of $S^{(i)}_{n.sym}(\alpha,\beta,T)$ with other $S_{n.sym}(\alpha,\beta,T)$ contributions, we propose phasing out this antiquated approximation.

2.2 Improved Numerical Operations

Recall that calculation of the scattering law given a continuous, solid-type spectra requires solving

$$S^{(s)}_{n.sym}(\alpha,\beta,T) = \mathrm{e}^{-\alpha\lambda_s}\sum_{n=0}^{\infty}\frac{1}{n!}\left[\alpha\lambda_s\right]^n \mathcal{T}_n(\beta) \tag{1.38}$$

where

$$\mathcal{T}_n(\beta) = \int_{-\infty}^{\infty}\mathcal{T}_1\left(\beta'\right)\mathcal{T}_{n-1}\left(\beta-\beta'\right)d\beta'. \tag{1.45}$$

These two equations are effective in illustrating how insufficient numerical methods can affect the final output $S_{n.sym}(\alpha,\beta,T)$ value. For example, NJOY's LEAPR module approximates the infinite sum in Eq. 1.38 as a sum from $n = 1...N$, where N is either specified by the user, or set to a default value of 100. Regardless of whether N is selected by the user or left to its default, this value stays constant for all α,β, and temperature values. Thus, to eliminate this arbitrarily chosen cutoff, the predefined summation

[1] Currently there are 34 files for thermal neutron scattering data inputs released in the ENDF/B-VIII library [17], and a handful of alternate inputs provided with NJOY documentation [3].

bound N is replaced with a tolerance-defined exit case (e.g. end summation when consecutive $S_{n.sym}(\alpha, \beta)$ values are within $\tau\%$ of each other). Further discussion regarding the summation limit and rate of convergence is provided in Sec. 5.2.

2.2.1 Nonuniform Phonon Distribution Energy Grid

Currently, LEAPR requires that the input phonon distribution be provided on a constant energy grid. A benefit to this restriction is that it facilitates the calculation of the convolution integral in Eq. 1.45 because $\beta - \beta'$ is ensured to be on the same grid as β. A non-uniform input frequency distribution grid is favorable, however, because it would allow increased precision on crucial parts (e.g. peaks) of the phonon distribution, without forcing prohibitively many points in flatter regions. Recall Fig. 1.1, which is a good example of the limitations of uniform phonon distribution spacing. In order to avoid the deprecated discrete oscillator approximation, the two higher energy peaks would need to be defined in the continuous phonon spectrum. So a fine grid would be required for the area surrounding those peaks, but a coarse grid would be preferred for the flat plateaus in the surrounding areas.

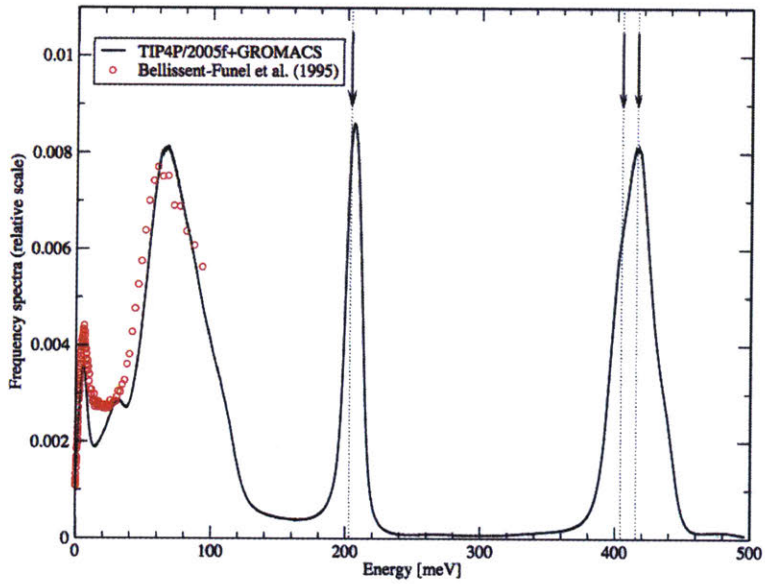

Figure 1.1: Phonon Distribution for H in H_2O [12]. The red points and the arrows represent measured data against which to compare the calculated spectrum. Of particular interest are the two peaks near 200 and 400 meV which, in typical NJOY LEAPR inputs, are approximated as discrete oscillators.

2.3 Implementation of $S(\alpha, \beta)$ Sampling into OpenMC

The sampling method developed by [10] is implemented into the OpenMC Monte Carlo neutron transport simulation code [16], both for validation purposes as well as to allow OpenMC users to make use of this improved scheme through the Python API. The API serves as a convenient interface with which to interact with OpenMC and to further facilitate neutron criticality calculations. Implementation of the sampling technique is used to compare the obtained energy and angle distributions with those generated using conventional methods (i.e. the THERMR module of NJOY).

Chapter 3

Accurate Representation of Phonon Distributions

3.1 Discrete Oscillator Approximation

The LEAPR module of NJOY, which prepares thermal scattering data via the scattering law, $S(\alpha, \beta, T)$, often approximates peaks in the phonon spectra as discrete oscillators and models them as weighted δ functions. This approximation, also known as the "Einstein crystal" approximation, is not a physically accurate representation of water. For instance, recall the phonon distribution for H in H_2O from Fig. 1.1, which was obtained using a molecular dynamics calculation. The peaks near 0.2 eV and 0.4 eV are quite unlike δ-functions, and a comparison between the δ-function distribution and the "true" distribution will be explored in Sec. 3.6. However, first we will consider how to replicate the discrete oscillator model. In the event that a user would want to avoid this approximation and instead apply the continuous phonon distribution treatment to those selected areas, it is crucial to verify agreement between these two methods. To test this, a simplified model for H in H_2O is used, which is modeled after Test Problem #9 in the NJOY 2016 release [3].

3.1.1 Problem Specifications

The test case used for this discrete oscillator discussion depicts a simplified H in H_2O model. The water is comprised of H-1 and O-16, and is held at $T = 296$ K. An input phonon spectrum is used for the solid-type continuous model, and two discrete oscillators are used to represent higher energy peaks. The phonon distribution and discrete oscillators, which are taken from Test #9 in NJOY 2016, are plotted in Fig. 3.1 [3].

The continuous phonon spectrum is defined as $\rho(\beta) = \rho(\Delta E/k_b T)$ for ΔE spanning from 0-0.16575 eV, where the energy grid is uniformly spaced in increments of 0.00255 eV. Unlike the original Test #9, no translational/diffusive contribution is considered ($\omega_t = 0$). The continuous weighting ω_s is set to 0.5, and the discrete oscillator energies and weights are provided in Table 3.1. Note that the listed weights satisfy the normalization

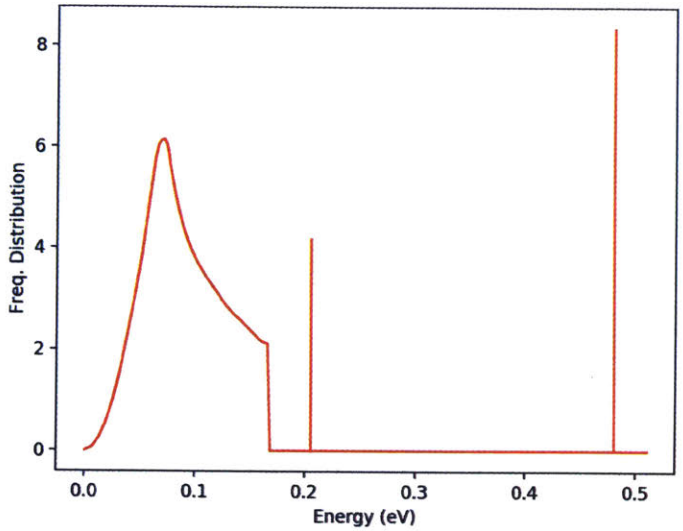

Figure 3.1: The phonon distribution for NJOY 2016 Test Problem 9 is shown above. It contains a continuous contribution, shown in the lower energy region, and two δ functions to approximate the higher energy peaks. Note that the δ functions are of arbitrary height relative to the continuous spectrum.

requirement stated in Eq. 1.32.

Energy (eV)	Weighting
0.205	0.166667
0.480	0.333333

Table 3.1: Energies and Weights for δ functions used in NJOY 2016 Test Problem 9

3.2 Representing Discrete Oscillators as Continuous Points

In order to allow users to avoid the δ function approximation that is commonly used in NJOY's LEAPR module, it is crucial to demonstrate similar behavior between how the solid-type continuous treatment vs. discrete oscillator treatment processes sharp peaks. The problem specifications detailed in Sec. 3.1.1 are considered, and the discrete oscillators are represented as thin triangles in the continuous spectrum. To allow for more flexible analysis, LEAPR's source code was translated from Fortran to C++. After presenting the frequency distributions that will approximate the peaks as triangles, the features of $S(\alpha, \beta)$ will be discussed, and the then the effect of the "triangle approximation" will be studied. The agreement between the translated C++ LEAPR and Fortran

LEAPR is described in Appendix C.1.

3.2.1 Replacing Discrete Oscillator δ Functions as Triangles

To verify that discrete oscillator treatment can be replicated by using increasingly thin triangles, each triangle must integrate to the weight of its corresponding δ function. Triangles of various widths (2,4,6,8, and 10 grid spaces) are used to replace both δ functions, and are plotted in Fig. 3.2. Additionally, a close-up of the 0.204 eV oscillator region is provided to illustrate a discrepancy between the triangle and oscillator locations[1].

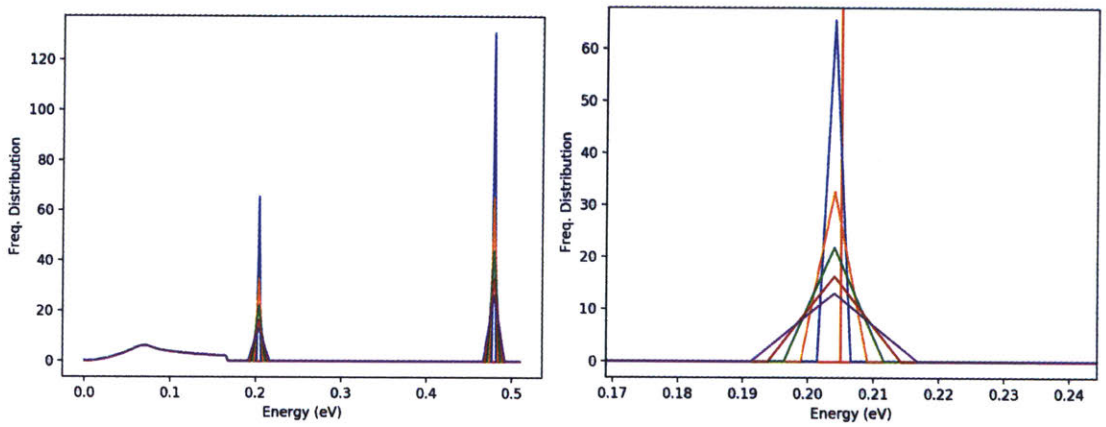

Figure 3.2: Phonon Distribution for H in H_2O, with oscillators replaced with phonon distribution triangles of various widths. The area under each triangle integrates to its corresponding δ function weight ω_i, and the lower energy continuous component integrates to the solid-type weight ω_s. A close-up of the 0.204 eV oscillator is provided. Note that due to the continuous spectrum being defined on a uniform grid, the triangles are not perfectly aligned with the δ function.

NJOY requires any continuous phonon distribution to be provided with respect to a uniformly-spaced energy grid. Thus, in Fig. 3.2, the centers of the triangles are not necessarily equal to the exact location of the δ functions that are specified in Table. 3.1. As a result of the discrepancy between discrete oscillator location and triangle center location, the oscillators energies are shifted slightly to align better with the $\Delta E = 0.00255$ eV grid to which NJOY is restricted. The δ function parameters presented in Table. 3.1 are amended to those in Table. 3.2. By slightly shifting the locations of the oscillators so that they are aligned with the triangles' grids, Fig. 3.2 becomes Fig. 3.3. The oscillator

[1]Note that the continuous component of the frequency spectrum in Fig. 3.2 looks significantly less pronounced than that shown in Fig. 3.1; this discrepancy is due to fact that Fig. 3.1 has arbitrary normalization (so as to show the continuous spectrum in full detail), whereas Fig. 3.2 represents the peaks such that their area integrates to their corresponding oscillator weights.

Energy (eV)	Weighting
0.204	0.166667
0.4794	0.333333

Table 3.2: Energies and Weights for δ functions, Amended to Align with Energy Grid

energies detailed in Table 3.2 are the problem specifications used for the remainder of this discussion.

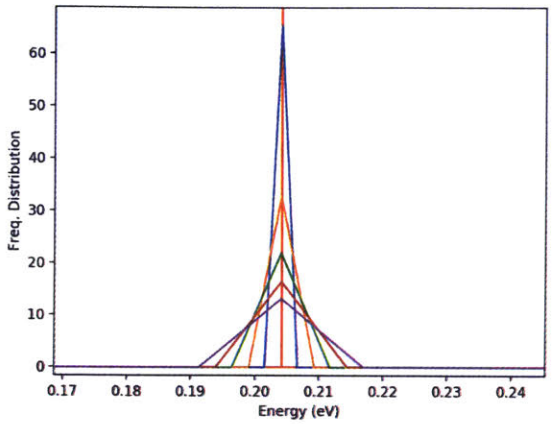

Figure 3.3: Phonon distribution for H in H_2O, with triangles approximating the oscillators. The oscillator locations are shifted to the locations listed in Table 3.2, so as to account for the offset due to restrictions in the $\rho(E)$ grid.

3.2.2 Features of $S(\alpha, \beta)$

Before proper analysis of the effect that different representations of the frequency distribution can have on $S_{n.sym}(\alpha, \beta)$, the scattering law and its features must first be briefly discussed. Fig. 3.4 shows the scattering law for H in H_2O, for a temperature of 296 K and an initial neutron energy of 1 eV. Only valid (α, β) combinations are plotted (given the aforementioned conditions of neutron energy and temperature).

Fig. 3.4 contains many sharp peaks, at specific β values. Using the material temperature $T = 296$ K and the definition of β from Eq. 1.17, these peaks are converted to eV. The peak locations, both β and eV values, are presented in Table 3.3, as well as the physical reasons for each peak.

Recall Eq. 1.57,

$$S_{n.sym}^{(s,1,2)}(\alpha, \beta) = \sum_{m=-\infty}^{\infty} A_{2,m}(\alpha) \sum_{n=-\infty}^{\infty} A_{1,n}(\alpha) S_{n.sym}^{(s)}(\alpha, \beta - n\beta_1 - m\beta_2) \tag{1.57}$$

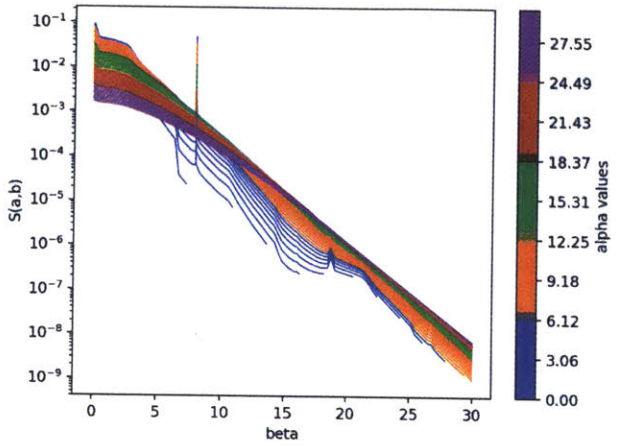

Figure 3.4: $S_{n.sym}(\alpha, \beta)$ for H in H_2O is shown. Both the α and β grids extend from 0.0 to 30, the temperature is set at 296 K, and the initial neutron energy is 1 eV. Note that only valid (α, β) combinations are plotted, which results in discontinuities of the lines.

β Locations of Peaks	ΔE Value (eV)	Origin
7.99	0.204	E_1
10.79	0.275	$E_2 - E_1$
15.99	0.407	$E_1 + E_1$
18.79	0.479	E_2
26.79	0.683	$E_1 + E_2$

Table 3.3: Locations of $S(\alpha, \beta)$ peaks from 3.4 that arise from discrete oscillators. Note that E_1 and E_2 correspond to the first and second discrete oscillator energy that were introduced in Table 3.2.

which illustrates the form of the non-symmetric scattering law, when the results of a continuous spectrum is combined with those of two oscillators, located at β_1 and β_2. This indicates the importance of β values that are integer linear combinations of oscillator locations β_1 and β_2.

3.3 $S(\alpha, \beta)$ Response to Continuous vs. Discrete Oscillator Representation

3.3.1 $S(\alpha, \beta)$ Response to Thin Triangle vs. Oscillator

This section is dedicated to exploring how well a thin triangle in the frequency spectrum mimics the behavior of a discrete oscillator, for the H in H_2O problem specifications previously defined. As mentioned in Sec. 3.1.1, the phonon grid is defined with a uniform energy spacing of $\Delta E = 0.00255$ eV, meaning that the thinnest triangle available has a total width of $2 \times \Delta E = 0.0051$ eV. For the remainder of Sec. 3.3.1, this minimum-width triangle will be the only triangle of focus, and the effects of changing triangle width will be explored in Sec. 3.3.2.

Fig. 3.5 shows the $S_{n.sym}(\alpha, \beta)$ grids generated by LEAPR, using both the discrete oscillator and the thin triangle phonon representation. The $S_{n.sym}(\alpha, \beta)$ grid is plotted against β for various α values. Note that the peaks near 16, 18, and 26 eV are significantly more pronounced in the triangle representation than they are in the discrete oscillator representation.

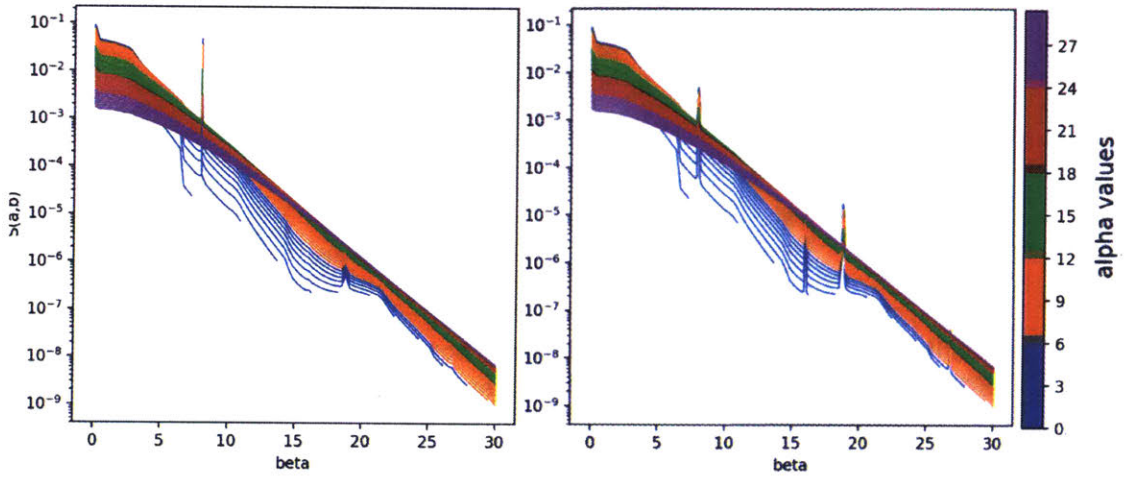

Figure 3.5: Two $S_{n.sym}(\alpha, \beta)$ tables are plotted above, the left grid assumes a δ function representation for the frequency distribution peaks, while the right plot represents said peaks as thin triangles. Note that representing peaks in the frequency spectrum as thin triangles as opposed to δ functions results in more pronounced peaks at higher β.

The absolute error and percent error between the discrete-oscillator scattering law and the triangle-approximated scattering law are plotted in Fig. 3.6. Note the significant errors that occur at the β values that are multiples of the oscillator energies (listed in Table 3.3).

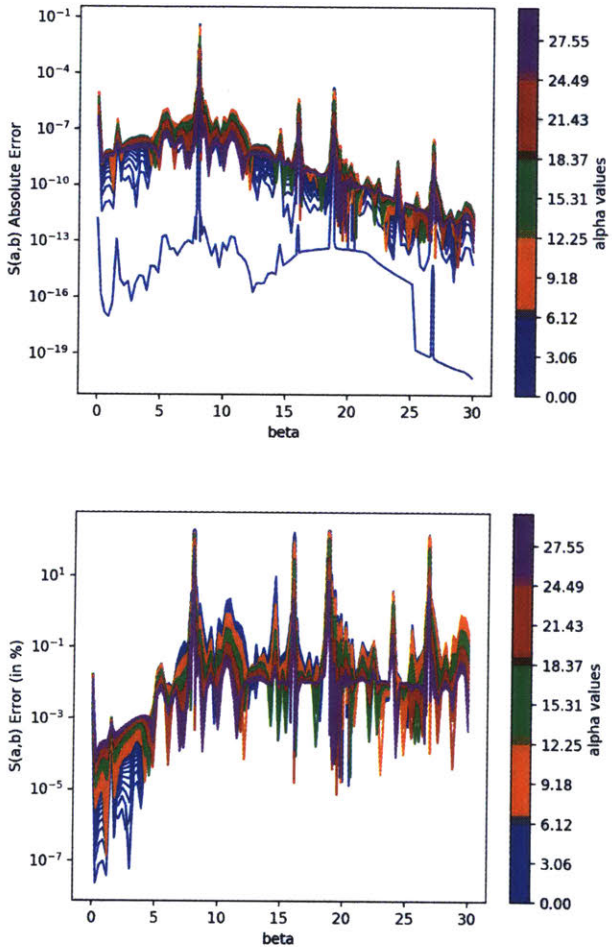

Figure 3.6: Absolute and percent error between discrete oscillator generated $S_{n.sym}(\alpha, \beta)$ and the thin triangle generated $S_{n.sym}(\alpha, \beta)$ are presented above.

Fig. 3.7 shows $S_{n.sym}(\alpha, \beta)$ zoomed in comparisons for the discrete oscillator representation (solid line) against the thin-triangle representation (dotted line), assuming an α value of 10.0. By contrasting these close-ups of the two outputs, it is apparent that the continuous representation of the peak has a wider spread than that of the discrete oscillator. This is to be expected, since the triangle needs three points in the frequency distribution to define its shape, while the δ function is defined at one particular point.

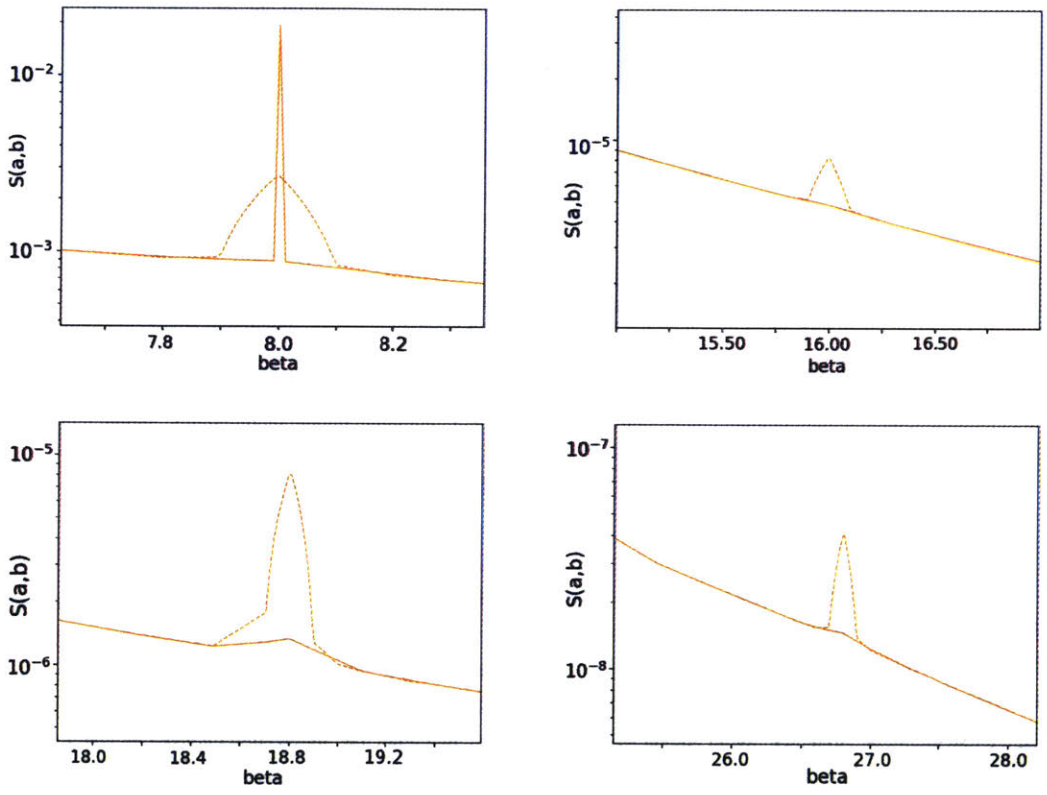

Figure 3.7: Close-up view of $S_{n.sym}(\alpha, \beta)$ is plotted above, where the discrete oscillator and thin triangle representations are shown using solid and dotted lines, respectively. This serves as an additional way of contrasting the two plots from Fig. 3.5. An α value of 10.0 is used here, since it is valid (i.e. in compliance with Eq. 1.61 for the entire β range considered).

3.3.2 $S(\alpha, \beta)$ Response to Changes in Triangle Size

Comparison of $S(\alpha, \beta)$ Values

Sec. 3.3.1 illustrates how substituting a thin triangle in for a discrete oscillator affects the $S_{n.sym}(\alpha, \beta)$ distribution for a large range of α and β values. The triangle in the phonon distribution has a width of two grid spaces, for a total of $2 \times \Delta E = 2 \times 0.00255 = 0.0051$ eV. Now we look to how the scattering law changes in response to triangles of various widths. These widths, in both number of grid spaces and eV, are displayed in Table 3.4.

Width (# grid points)	Width (eV)	Height for 0.204 eV Peak	Height for 0.4794 eV Peak
2	0.0051	65.35960	130.71882
4	0.0102	32.67980	65.35941
6	0.0153	21.78653	43.57294
8	0.0204	16.33990	32.67970
10	0.0255	13.07192	26.14376

Table 3.4: Widths of triangles used to study $S_{n.sym}(\alpha, \beta)$ response to triangle aize. Note that these triangles, which were originally presented in Fig. 3.3, have heights defined so as to ensure that their area integrates to the correct oscillator weight (weights listed in Table 3.2).

In a study conducted by [12], the vibrational frequency spectrum of H in H_2O was calculated using a molecular dynamics simulation, and the resultant scattering properties were contrasted against those obtained using the simple spectrum discussed here. The calculated frequency spectrum was originally introduced in Fig. 1.1, and the two higher energy peaks near 0.2 eV and 0.48 eV had base widths of approximately 0.03 eV and 0.07 eV, respectively. Thus, the triangles used to approximate the frequency distribution defined in Table 3.4 are thinner than those that would appropriately approximate the peaks obtained in the [12] study. This is of interest to note but will not be discussed further, since the current discussion is focused on mimicking discrete-oscillator behavior.

The triangles described in Table 3.4 are used in the H in H_2O input and, for a given α, the resultant scattering laws can be compared against the output generated using the discrete oscillator approximation. This comparison is shown in Fig. 3.8, assuming an α value of 0.5, and a β range centered about the $\beta = 7.99$ region, so as to highlight the effects of the peak introduced in Fig. 3.4.

Comparison of $S(\alpha, \beta)$ Differences

A comparison of how the scattering law $S_{n.sym}(\alpha, \beta)$ responds to changes in triangle width is presented in Fig. 3.8. Here, we look at the total difference between the triangle-

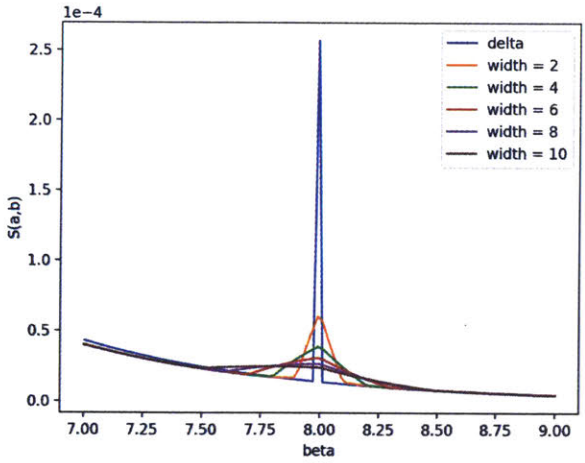

Figure 3.8: Response of $S_{n.sym}(\alpha, \beta)$ to triangles of various size, for $\alpha = 8.1$. The β range is focused on $\beta = 7.99$. Note that as the triangles decrease in width, the resultant scattering laws better resemble that of the discrete oscillator.

generated outputs and the discrete oscillator output, $\Delta_{total,i}$, which is defined as

$$\Delta_{total,i} = \int \int \left| S^{\delta}_{n.sym}(\alpha, \beta) - S^{i}_{n.sym}(\alpha, \beta) \right| \, d\beta \, d\alpha. \tag{3.1}$$

$S^{\delta}_{n.sym}(\alpha, \beta)$ and $S^{i}_{n.sym}(\alpha, \beta)$ are the scattering laws generated using a discrete oscillator and a triangle of width i, respectively. $\Delta_{total,i}$ is computed for each triangle described in Table 3.4, the values of which are then plotted in Fig. 3.9. As was the case for Fig. 3.8, the β grid is centered about the $\beta = 7.99$ peak.

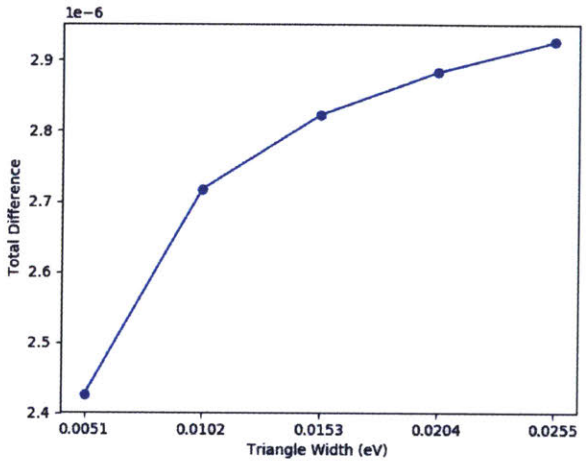

Figure 3.9: Total $S_{n.sym}(\alpha, \beta)$ difference between triangles of various widths and discrete oscillator approximation. The error is computed using the $S_{n.sym}(\alpha, \beta)$ values from Fig. 3.8, summed across all α values. Note that as triangle width decreases, so does the total accumulated error.

3.4 Comparison of Resultant Cross Section

It was shown in Sec. 3.3 that different representations of the vibrational spectrum affect the scattering law $S(\alpha, \beta)$. However, proper analysis requires a closer look into a more physically meaningful value, such as the cross section. Thus, in this section, we continue the discussion to now include the incoherent inelastic cross section, which we recall is related to the scattering law by

$$\sigma\left(E \rightarrow E', \mu\right) = \frac{\sigma_b}{2k_bT}\sqrt{\frac{E'}{E}}S_{n.sym}(\alpha, \beta, T). \tag{1.1}$$

3.4.1 Features of the Cross Section

First, we look at the cross section for a 1 eV neutron colliding with H in H_2O at 296 K. E' varies from $0 \rightarrow 1.5$ eV, and the scattering cosine μ is allowed to vary from $-1 \rightarrow 1$. The bound cross section σ_b has a value of 20.449 b, the continuous frequency distribution is taken from NJOY's Test #9 (shown in Fig. 3.1), and the discrete oscillator representation detailed in Table 3.2 is used to represent the higher energy peaks in the frequency distribution. The resultant cross section is shown in the top left plot of Fig. 3.10. Note that the large peak at 0.796 eV is a result of the 0.204 eV discrete oscillator (in that the 1 eV neutron lost 0.204 eV of energy, bringing it to a $E' = 0.796$ eV). A zoomed-in view of this 0.796 eV peak is provided on the top right of Fig. 3.10, which illustrates that the cosine values most affected by this 0.204 eV oscillator are μ values greater than 0.6. In fact, observing the plot in the lower left corner of Fig. 3.10 shows the unlikely nature of backscattering, as the cross sections decrease significantly as $\mu \rightarrow -1$.

To better see the other peaks, a zoomed in view is also provided in Fig. 3.10. In this close-up view, we can clearly see the peak at $E' = E = 1$ eV, where neutron energy is conserved. A less sharp, but still well defined peak exists centered about $E' = 0.93$ eV. This duller peak is due to the continuous frequency distribution that was introduced in Fig. 3.1, which has a rounded peak near $0.07 - 0.08$ eV. Finally, we see the effects of the second δ function (which has a location in energy at 0.4794 eV). This second oscillator causes the subdued peak at $E' = 0.52$ eV. The latter δ function has a muffled effect, since in Eq. 1.1, the $\sqrt{E'}$ factor favors higher values of E'.

3.4.2 Effect of Triangle Width on Cross Section

The cross sections shown in Fig. 3.10 were calculated using the discrete oscillator approximation. Now, the cross sections are calculated using triangles of various sizes to represent the peaks, similar to the analysis performed in Sec. 3.3.2. For triangles of 2-10 grid spaces in width, the $S_{n.sym}(\alpha, \beta)$ grids are computed and used to calculate the incoherent scattering cross section. The percent difference between these triangle representations and the discrete oscillator representation, along with their respective cross sections, are plotted in Figs. 3.11-3.12, assuming $\mu = 0.5$ and $\mu = 0.9$, respectively. A very prominent peak appears in Fig. 3.12 at $E' = 0.796$ eV, which as previously mentioned is due to the

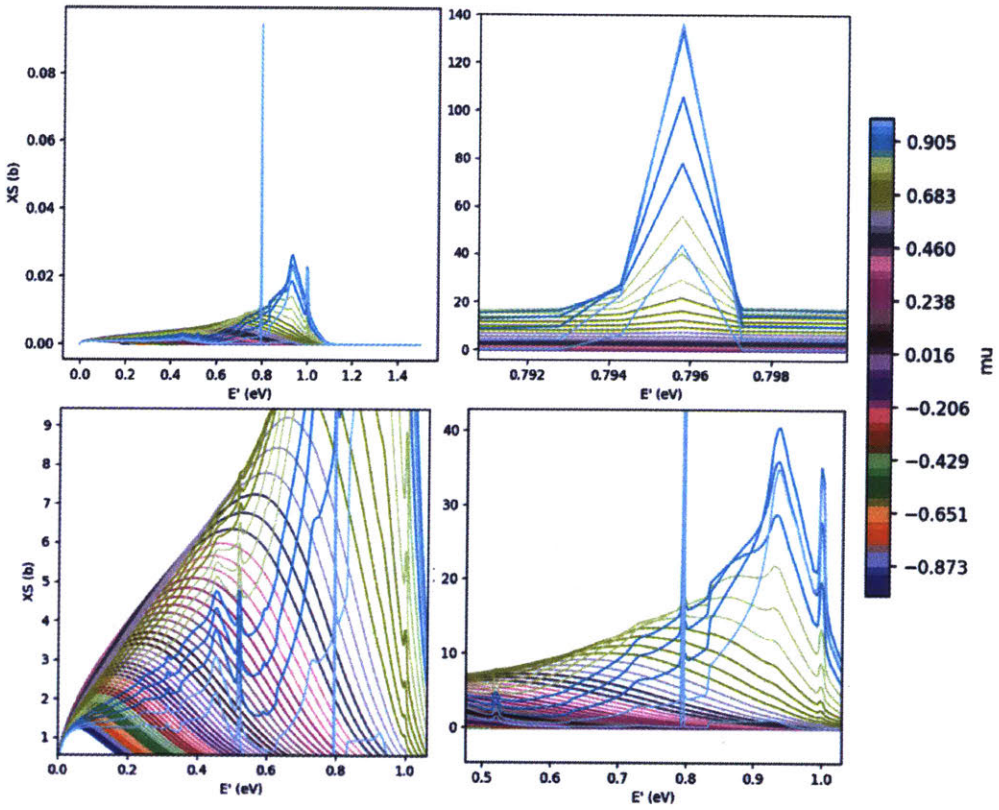

Figure 3.10: The incoherent cross section for H in H_2O is shown for various outgoing energies and angles, as calculated using the discrete oscillator approximation. Incoming neutron energy is 1 eV.

0.204 eV oscillator (since the incoming neutron energy has 1 eV). A closer view of this peak is provided in Fig. 3.13.

There are many sharp peaks in the percent difference between the discrete oscillator treatment and the triangular peak treatment, as shown in Fig. 3.11. These differences appear near the integer multiples of the discrete oscillator locations that were first identified in Table 3.3. These discrepancies between the two treatments was first introduced in Sec. 3.3.1, and will be further explored in Sec. 3.5.

While Figs. 3.11-3.12 show that thinner triangles tend to have larger peaks of error when compared to the δ function treatment, the thinner triangles actually tend to approach the δ function behavior. To see this, we look at Fig. 3.14, which plots the absolute difference integrated across all outgoing energies E' (for various angles μ and triangle widths). We see that while thin triangles experienced larger peaks of error when compared to the discrete oscillators, the wider triangles had more accumulated error in total, and that for all cosines, thinner triangles better mimic the discrete oscillator behavior overall.

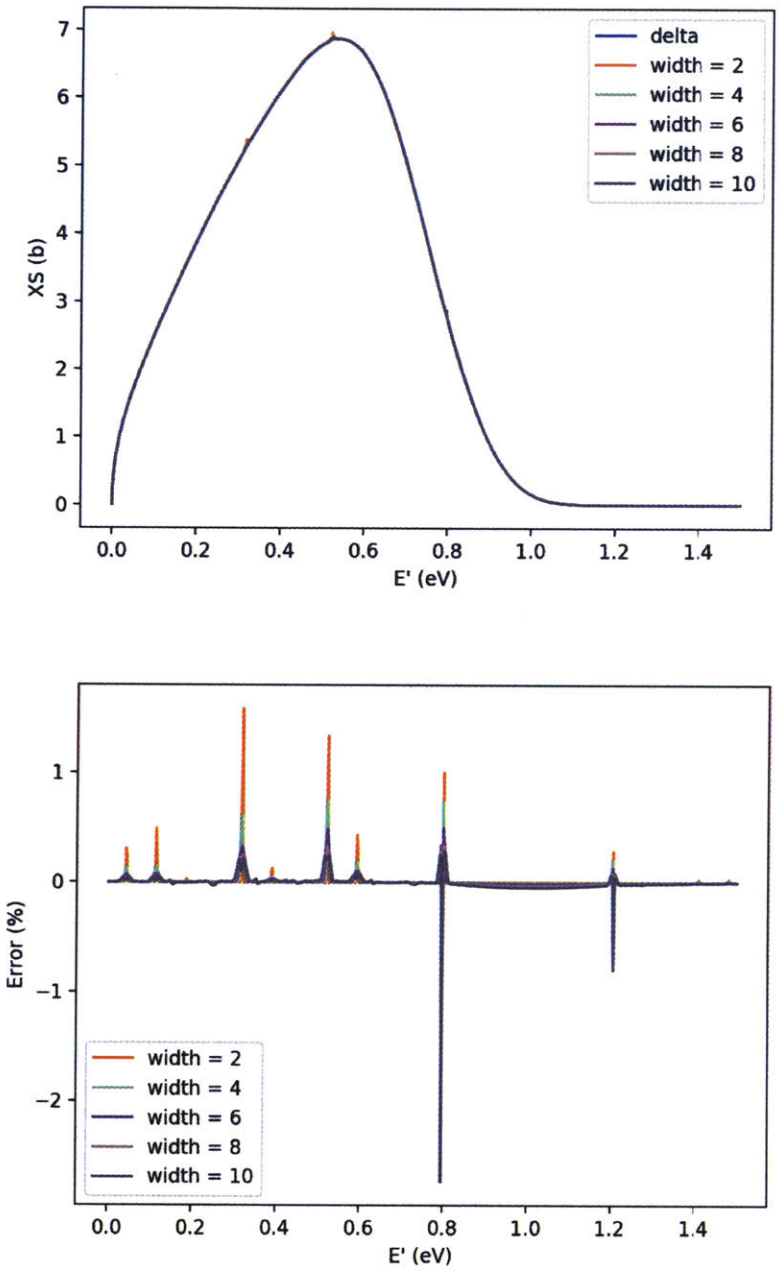

Figure 3.11: The cross sections, as generated by the δ-function approximation as well as by various triangle representations, are shown on the left, with the relative differences shown on the right. Both plots assume a scattering cosine $\mu = 0.5$. Five triangles of widths equal to 2-10 grid spaces (width = # Grid Spaces $\times$ 0.00255 eV) are considered, and compared to the discrete oscillator representation.

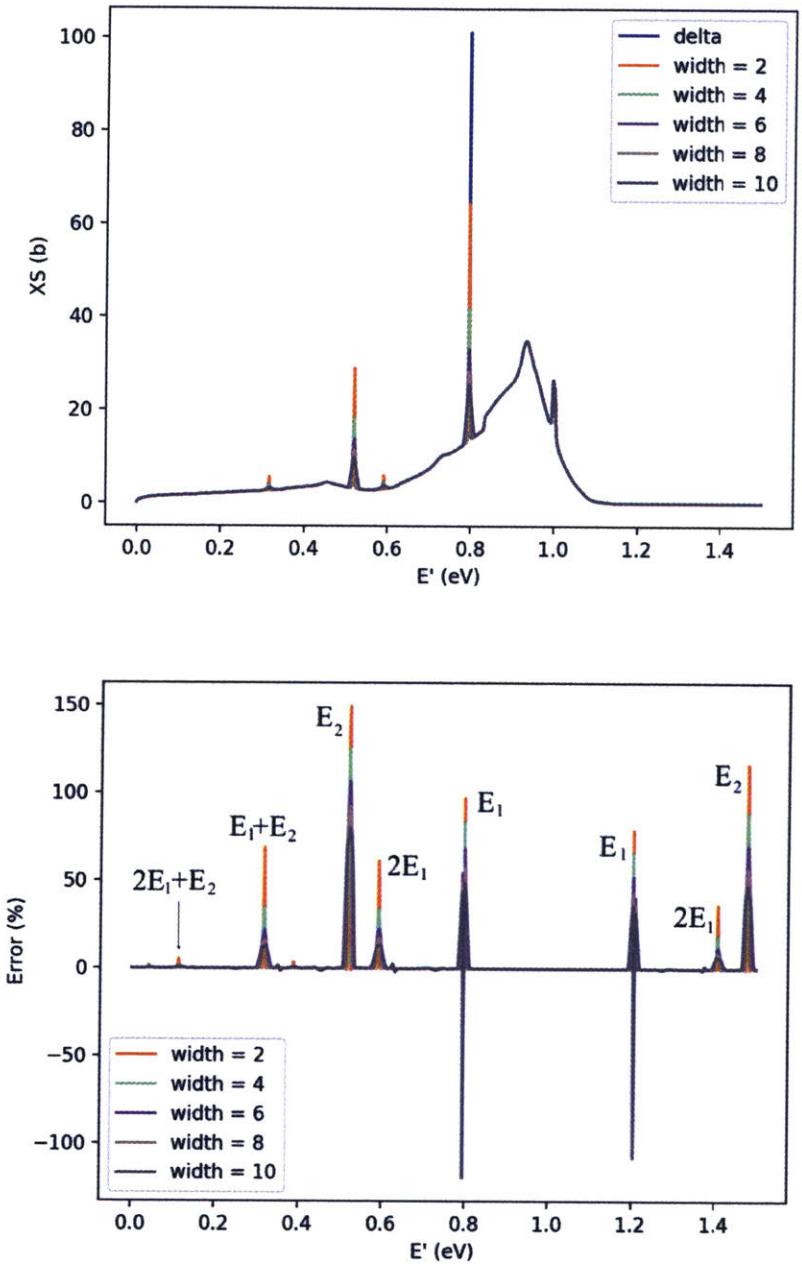

Figure 3.12: The cross sections, as generated by the δ-function approximation as well as by various triangle representations, are shown on the left, with the relative differences shown on the right. Both plots assume a scattering cosine $\mu = 0.9$. The percent difference plot includes labels for each major peak, indicating which combination of the discrete oscillators prompted its existence.

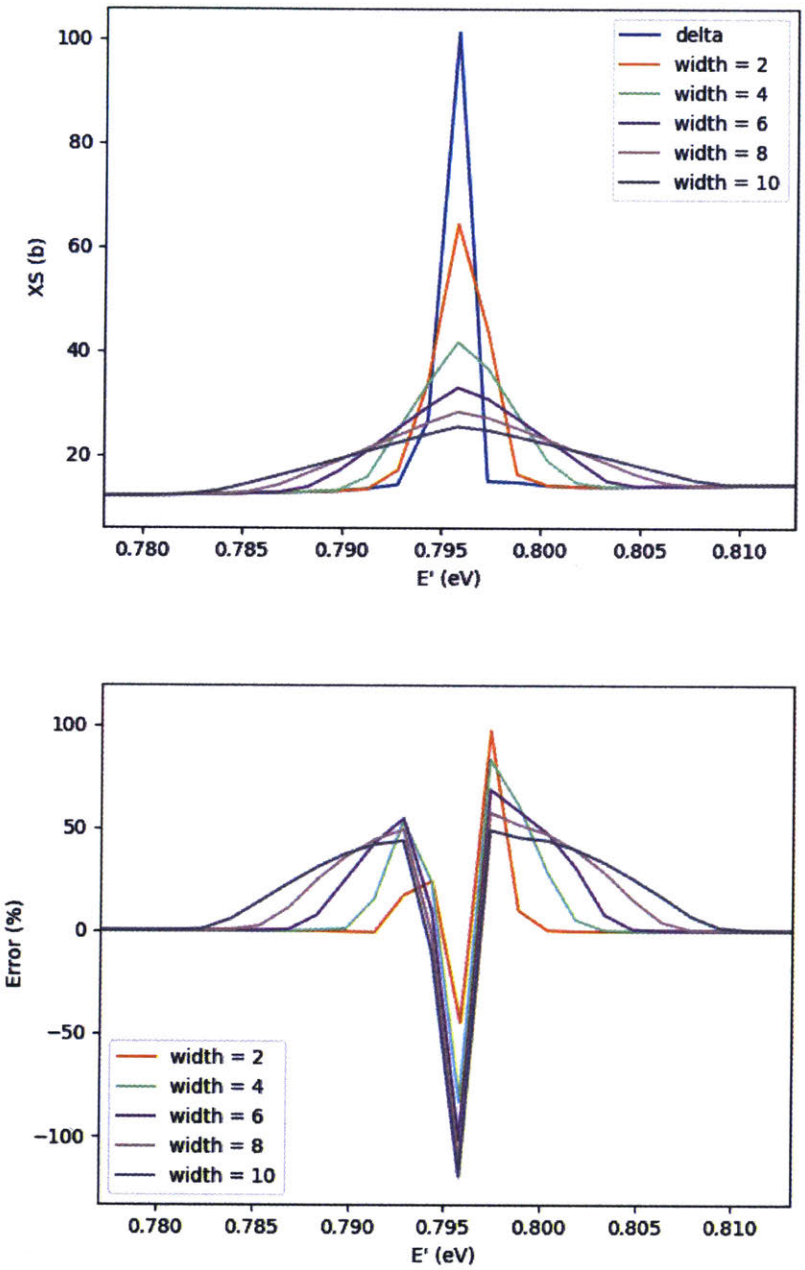

Figure 3.13: The cross sections, as generated by the δ-function approximation as well as by various triangle representations, are shown to the left. Percent difference between the cross sections generated using the discrete oscillator representation vs. triangular peaks in the frequency distribution are shown on the right. Both plots assume a scattering cosine $\mu = 0.9$, and are centered about the peak caused by the 0.204 eV oscillator ($E' = 0.796$ eV).

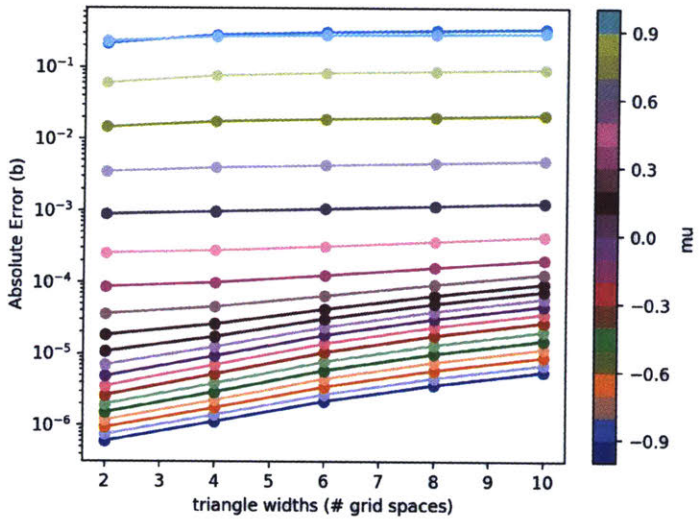

Figure 3.14: Absolute difference between discrete oscillator generated cross sections and thin triangle generated cross sections, integrated over all outgoing energies E', is shown above.

3.5 Discrepancy Between Continuous and Discrete Oscillator Treatment

The discrepancy between the discrete oscillator treatment and the thin triangle treatment first appeared when comparing $S_{n.sym}(\alpha, \beta)$ in Figs. 3.5-3.7, and was again apparent when comparing the generated cross sections, such as those shown in Fig. 3.12. However, since all cases thus far have compared inherently different models (a thin triangle vs. a δ function), it is not yet apparent whether the observed discrepancies are due to the methodology used to evaluate the scattering law, or whether they are rather the result of the triangles' finite size.

As shown in Sec. C.2, the equations representing the discrete oscillator treatment are a direct simplification of the those representing the generic, continuous distribution case, with the only additional simplification being that the frequency distribution is equal to a δ function, $\rho(\beta) = \delta(\beta - \beta_i)$. Thus, it is expected that the two methods are equivalent when the phonon expansion is performed. To see this, recall both the original definition of the $\gamma(\hat{t})$ function,

$$\gamma(\hat{t}) = \alpha\lambda_s - \alpha \int_{-\infty}^{\infty} P(\beta) \mathrm{e}^{-\beta/2} \mathrm{e}^{-i\beta\hat{t}} \, d\beta, \tag{1.33}$$

the negative exponential of which is

$$\mathrm{e}^{-\gamma(\hat{t})} = \exp\left[-\alpha\lambda_s - \alpha \int_{-\infty}^{\infty} P(\beta) \mathrm{e}^{-\beta/2} \mathrm{e}^{-i\beta\hat{t}} \, d\beta\right]. \tag{3.2}$$

This differs from the exponential of $-\gamma(t)$ as defined by the phonon expansion,

$$\mathrm{e}^{-\gamma(\hat{t})} = \sum_{n=0}^{\infty} \left(\mathrm{e}^{-\alpha\lambda_s} \frac{1}{n!} \left[\alpha \int_{-\infty}^{\infty} P(\beta') \mathrm{e}^{-\beta'/2} \mathrm{e}^{-i\beta'\hat{t}} \, d\beta' \right]^n \right) \tag{1.35}$$

which expands the exponential of the the integral as an infinite sum. If the aforementioned frequency spectrum, $\rho(\beta) = \delta(\beta - \beta_i)$ is provided to both Eq. 1.33 and Eq. 1.35 for given α and β_i values, the results are identical. To see their shape, the exponential is plotted against time in Fig. 3.15, assuming $\alpha = 3.0$ and a single discrete oscillator located at $\beta_i = 0.5$.

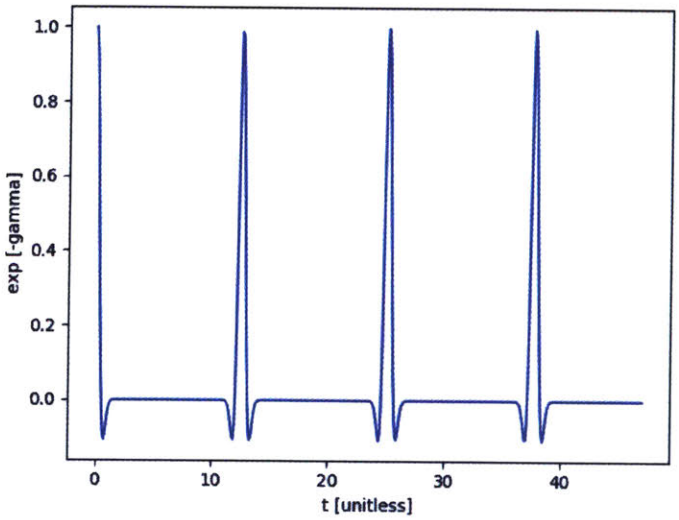

Figure 3.15: The exponential of $-\gamma(\hat{t})$ is plotted against unitless time $\hat{t}$, assuming $\rho(\beta) = \delta(\beta - 0.5)$ and $\alpha = 3.0$.

We now aim to characterize how well the $-\gamma(t)$ exponential in Fig. 3.15 is approximated by thin triangles in the input frequency spectrum $\rho(\beta)$. To accomplish this, Eq. 1.35 is numerically solved using phonon distributions that approximate the $\beta_i = 0.5$ oscillator by triangular peaks of various widths ($\Delta\beta = 5 \times 10^{-4}$ to 5×10^{-2}). The corresponding exponentials of $-\gamma(t)$ are plotted in Fig. 3.16. Note that as the width of the triangles decrease, the resultant exponential increasingly resembles the form of the discrete oscillator results from Fig. 3.15.

To further observe the effect that triangle size has on the resultant $-\gamma(t))$ exponential, the absolute difference between the discrete oscillator frequency distribution (Fig. 3.15) and the triangle frequency distribution (Fig. 3.16) is shown in the first plot of Fig. 3.17. The second plot in Fig. 3.17 shows how the absolute error changes in response to triangle widths, for a given value of $\hat{t}$. The $\hat{t}$ values chosen are the peaks near $\hat{t}$=12, 25, and 37. Note that Fig. 3.17 shows that for all three peaks considered, the decreasing triangle width steadily and significantly improves accuracy, thus supporting the prediction that the discrete oscillator behaviour can be replicated by using increasingly thin triangular peaks in the input frequency distribution.

The inability of the thin triangles to appropriately replicate discrete oscillator behavior in previous sections (e.g. when considering the scattering law in Sec. 3.3 or the cross section in Sec. 3.4) is likely due to the limitation on triangle thickness imposed by LEAPR. Note that in Fig. 3.17, close representation of the discrete oscillator $-\gamma(t)$ exponential was first obtained when the triangle width was near $\beta = 5 \times 10^{-3}$, which at room temperature corresponds to an energy difference of 10^{-4} eV. As mentioned in Sec. 3.1.1, the uniformly spaced input frequency distribution had a set energy difference of 0.00255 eV, which is

over 25 times larger than the adequate value of 10^{-4}. Thus, we find that a thin triangle can appropriately mimic the behavior of a δ-function in the input frequency distribution, but this is not feasible unless a non-uniform grid is allowed. Concluding remarks will be provided in Sec. 3.7, where the merit of the discrete oscillator approximation will be further discussed.

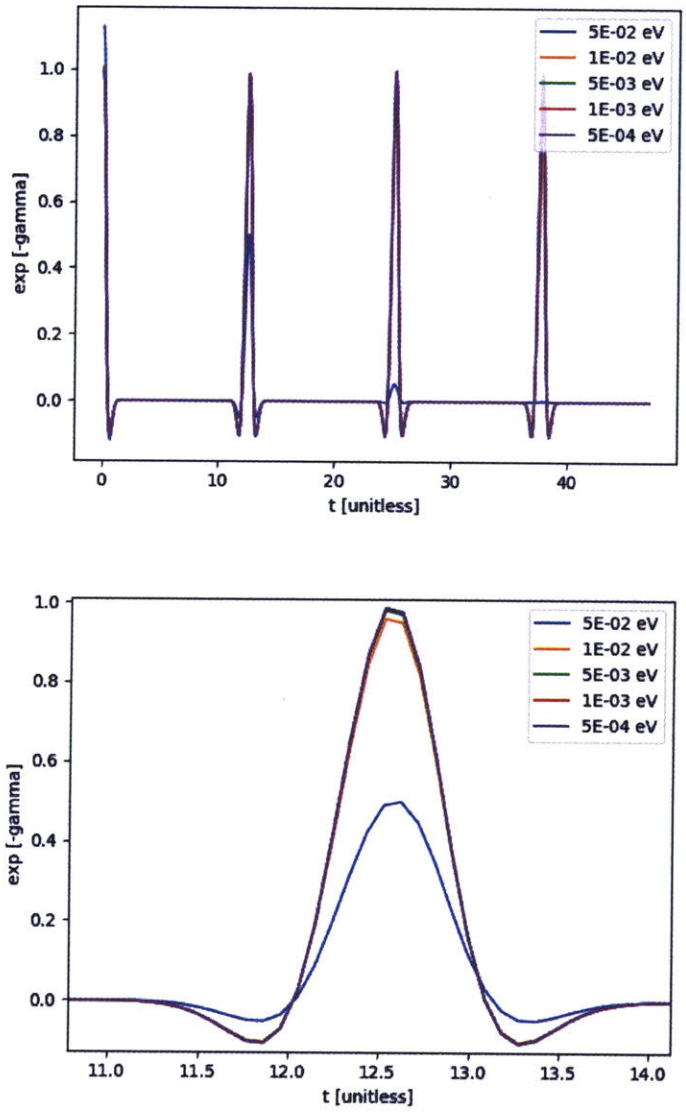

Figure 3.16: The exponential of $-\gamma(\hat{t})$ is plotted against unitless time $\hat{t}$, for a frequency spectrum where the discrete oscillators are represented as thin triangles of various widths. The latter plot is a zoomed-in view of the peak near the $\hat{t} = 12.5$ region.

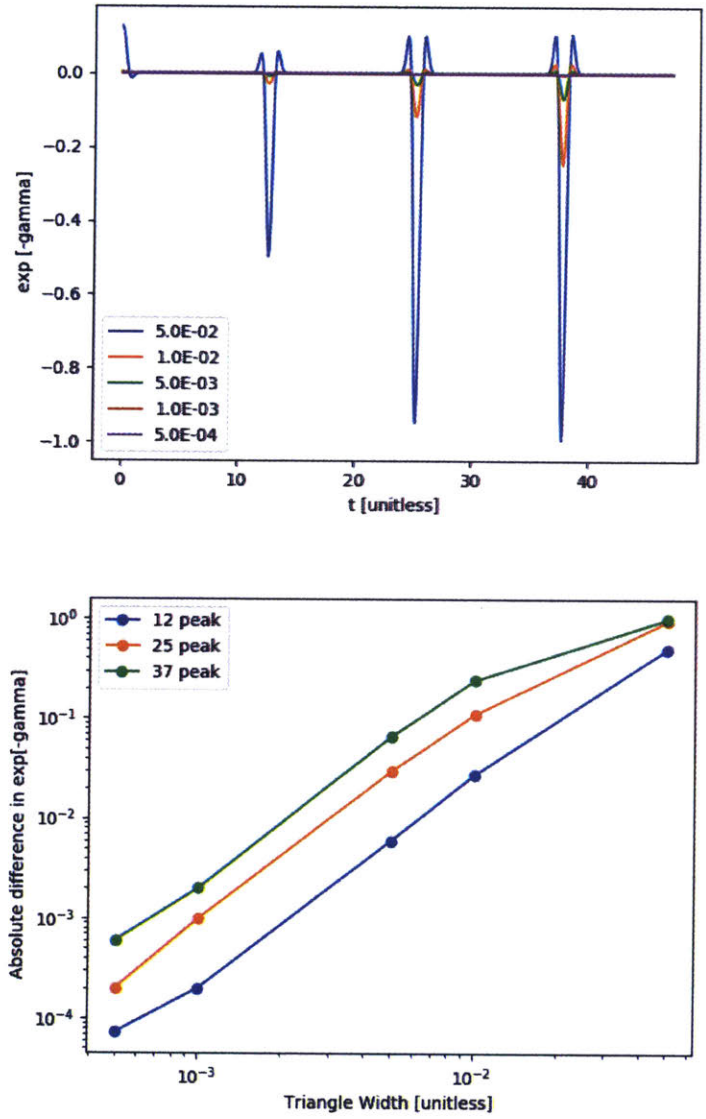

Figure 3.17: The first plot shows the absolute difference in $\exp[-\gamma(t)]$ as computed using the thin triangle approximations when compared against that computed using the discrete oscillator approximation. The second plot shows how the absolute error changes in response to triangle width, for three given $\hat{t}$ peaks ($\hat{t} \approx 12, 25, 37$).

3.6 Effects of The Discrete Oscillator Approximation

To understand the effects of the discrete oscillator approximation, we compare the full H in H_2O model against its discrete oscillator counterpart, both of which were published by [12] (note that this reduced model differs from the NJOY Test #9 example). The full model was originally introduced in Fig. 1.1.

Data from [12] was collected using the digitization tool *WebPlotDigitizer* [18]. The resultant phonon distributions were converted to a uniform grid, as is required by LEAPR, and are shown in Fig. 3.18. The δ-functions of the reduced model (which take the place of the higher energy peaks) are also included in Fig. 3.18, but note that the heights of the δ-functions are arbitrary. The apparent discrepancy between the full and reduced

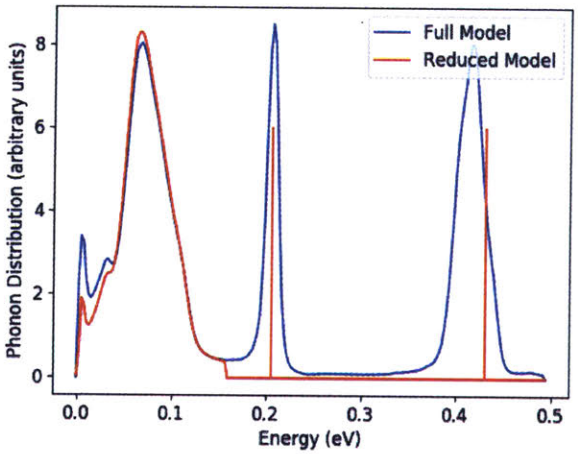

Figure 3.18: Phonon distributions comparing the full and simplified CAB models are shown above [12]. The full CAB model is normalized to unity and has no diffusion or translation. For the reduced model, the continuous component is normalized to 0.522421, with a translational weight of 0.008605 and diffusion coefficient of 4.060575. The discrete oscillators of the reduced model are also shown (heights are arbitrary).

models in the low energy region (near 0.01 eV) is due to the fact that the reduced model has a diffusive/translation component which is not represented in the peak, whereas the full model does not have a diffusive component[2].

The phonon distributions in Fig. 3.18 were provided to LEAPR, which processed and returned the negative side of the non-symmetric scattering laws, $S_{n.sym}(\alpha, -\beta)$. Both

[2]LEAPR gives the option for a diffusive component to be considered while processing a liquid moderator. This diffusive component has a translational weighting ω_t and a diffusion coefficient c, and was briefly introduced in Sec. 1.3.1

of these cases assumed a temperature of 296 K and used identical α and β grids. The resultant $S_{n.sym}(\alpha, -\beta)$ curves are plotted in Fig. 3.19 against β, for various α values.

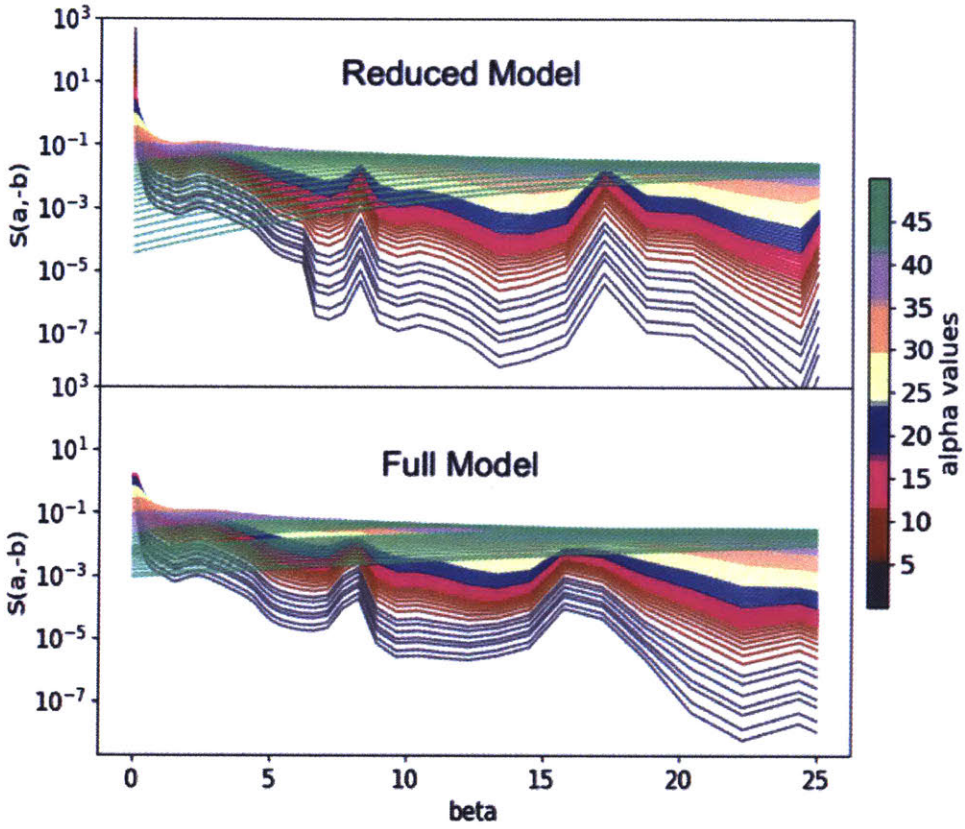

Figure 3.19: The negative side of the non-symmetric scattering laws $S_{n.sym}(\alpha, -\beta)$ are plotted above, as generated using the Test #9 and CAB phonon distributions.

Note that the shape and magnitudes of scattering law peaks are significantly different between the two models, as well as the overall trends. Prominent disagreement between the two models appears near $\beta = 8$ and 17, which occur due to the peaks/δ-functions in the phonon distribution. The two oscillator locations are at 0.205 eV and 0.43 eV, which at room temperature correspond to β =8.2 and 17.2, respectively. Note that the reduced model also significantly overestimates the near-elastic scattering.

These scattering laws are used to calculate the cross sections for various scattering cosines μ, shown in Fig. 3.20. The cross section plots were generated assuming an incoming neutron energy of 0.5 eV and, as before, a room temperature scattering material at T = 296 K. The top plot in Fig. 3.20 shows the scattering cross section, where the bottom plot shows the absolute difference (reduced model minus full model).

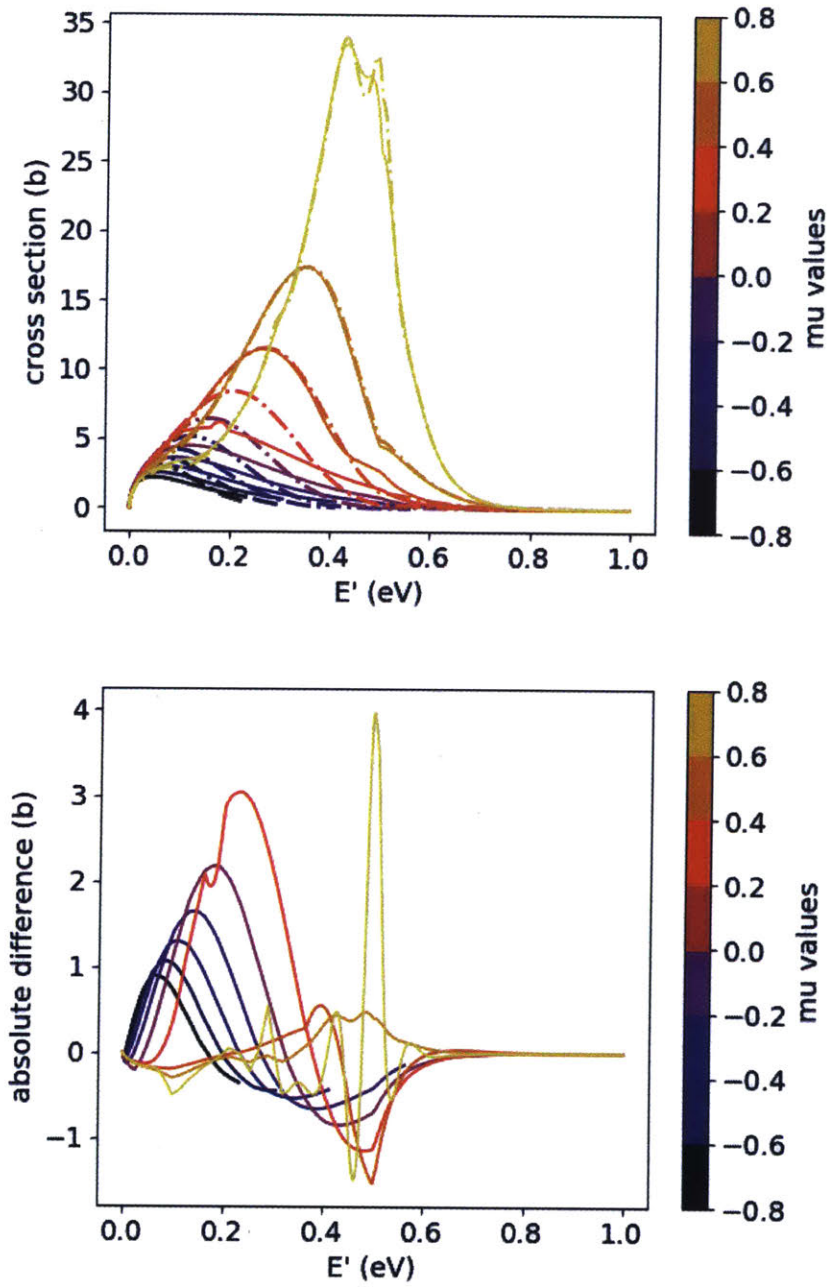

Figure 3.20: Scattering cross section (top) and absolute difference (bottom) comparing the full and reduced H in H_2O models, plotted against outgoing energy E' for various scattering cosines μ. An incoming energy of 0.5 eV is assumed. In the cross section plot, dotted and solid lines correspond to the reduced and full model, respectively. The absolute difference in the bottom plot is reduced model minus full model.

Note that in Fig. 3.19, the discrete oscillator model follows the forward scattering distributions rather well, but begins to significantly overestimate the scattering cross section for $\mu < 0.2$. To better see the discrepancy between the two models, the percent error is plotted in Fig. 3.21.

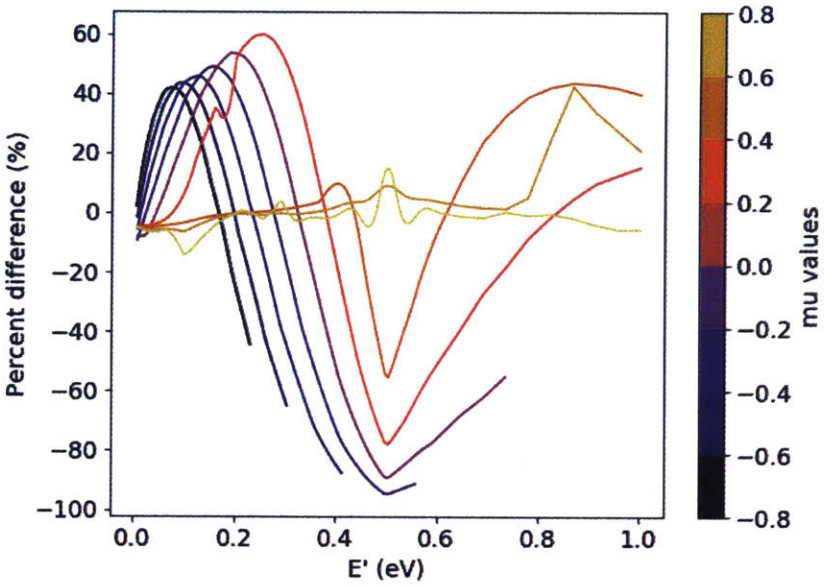

Figure 3.21: The percent difference between the scattering cross sections from the full and reduced H in H_2O models are plotted against outgoing energy E' for various scattering cosines μ. An incoming energy of 0.5 eV is assumed.

3.7 Validity of Abandoning Discrete Oscillator Approximation

The LEAPR module allows for peaks in the input frequency spectrum to be approximated as weighted δ functions, in what is called the discrete oscillator approximation. This approximation does not represent physics and its computational benefits are severely limited by the requirement that the discrete oscillator contribution to the scattering law must be convolved with preexisting contributions. These disadvantages serve as incentives to abandon the discrete oscillator approximation. However, if a user wanted to replicate the results of a system that was approximated using the discrete oscillator approximation, it is important to show that they could arrive at a similar result by using triangular peaks in the frequency spectrum. This chapter aimed to show that such replication was possible.

Replacing a discrete oscillator by a thin triangle in the vibrational spectrum results in similar scattering laws, as shown in Figs. 3.5-3.6. There are key disagreements, however, near linear combinations of the discrete oscillator locations, as shown in Fig. 3.7. These disagreements propagated to the sampled cross sections, which were shown in Figs. 3.11-3.12.

After further analysis using a simplified model of a single discrete oscillator, the behavior of the scattering system with increasingly thin triangles was found to approach that of a discrete oscillator, which was shown in Figs. 3.16-3.17. This agreement is to be expected since, as shown in Sec. C.2, the equation of the discrete oscillator approximation is a direct simplification of the continuous phonon expansion representation. Adequate replication of the discrete oscillator approximation, however, required that the triangle used to approximate the discrete oscillator be very thin. The only way such detail could be feasible is if the input frequency spectrum were be provided on a non-uniform grid.

In these concluding remarks, it is crucial to reiterate that the discrete oscillator representation is an approximation of the continuous treatment. The purpose of this discussion is, again, to illustrate that if the discrete oscillator option were to be abandoned, its behavior could still be adequately reproduced using triangles in the phonon distribution.

Chapter 4

Sampling of $S(\alpha, \beta)$

4.1 PDFs and CDFs for H in H_2O

Use of the sampling technique detailed in Sec. 1.4.3 requires construction of probability density functions and cumulative density functions for α and β. Secs. 4.1.1-4.1.2 introduces the PDFs and CDFs for H in H_2O, while Sec. 4.1.3 delves further into their dependence on temperature. All $S_{n.sym}(\alpha, \beta)$ grids shown and used here were calculated assuming the discrete oscillator approximation but the methodology would remain the same regardless of the selected representation.

4.1.1 PDF and CDF in α

Due to the low energy inherent to thermal neutrons, their scattering behavior is highly dependent on the target's temperature. The fitting approach developed by [10] would prove useful in reducing the burden of preprocessing thermal scattering data for many different temperatures. Thus, to obtain the PDFs and CDFs for H in H_2O, an equally spaced α grid that spans $0.01 \leq \alpha \leq 60.0$ with $\Delta\alpha \approx 0.12$ is provided to LEAPR with a specified β value of 10.1. The resultant $S_{n.sym}(\alpha, \beta)$ values are used in Eq. 1.69 to obtain the probability density function,

$$h(\alpha|\beta, E, T) = \frac{S_{sym}(\alpha, \beta, T)}{\int_{\alpha_{\min}}^{\alpha_{\max}} S_{sym}(\alpha', \beta, T) d\alpha'} \tag{1.69}$$

which can then be used in Eq. 1.71,

$$H(\alpha|\beta, E, T) = \int_{\alpha_{\min}}^{\alpha} h\left(\alpha'|\beta, E, T\right) d\alpha' \tag{1.71}$$

to obtain the CDF. The PDF and CDF for various temperatures are shown in Figs. 4.1-4.2, and were generated using the methods outlined in Algorithm 1.

Figs. 4.1,4.2 are for the specific case of $\beta = 10$ and replicate the results originally from [10]. To see the effect that changing β has on the α PDF and CDF curves, Fig. 4.3 plots the H in H_2O α PDFs and CDFs at 650 K, for various values of β.

Algorithm 1 Calculate α CDF while restricting α grid

Given: Defined $\alpha_{vec}, \beta_{vec}, E, T, S_{n.sym}(\alpha, \beta)$
for T in Temperatures **do**
  $\alpha_{vec} = [\alpha_{\min}, \ldots, \alpha_{\max}]$
  Area = Integrate $S_{n.sym}(\alpha, \beta, T)$ from $\alpha_{\min} \rightarrow \alpha_{\max}$
  for α in α_{vec} **do**
    $h(\alpha|\beta, E, T) = S_{n.sym}(\alpha, \beta, T))/\text{Area}$
    $H(\alpha|\beta, E, T) = H(\alpha - 1|\beta, E, T) + h(\alpha|\beta, E, T)$
  end for
end for

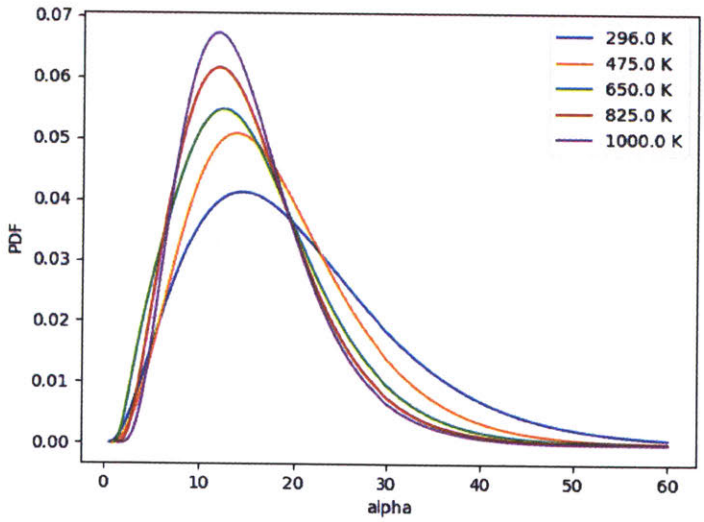

Figure 4.1: PDF in α for H in H_2O, given $\beta = 10$, for various temperatures.

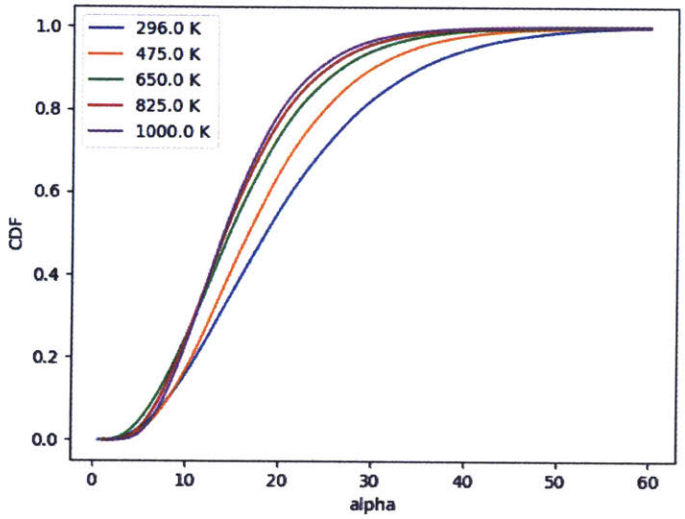

Figure 4.2: CDF in α for H in H_2O, given $\beta = 10$, for various temperatures.

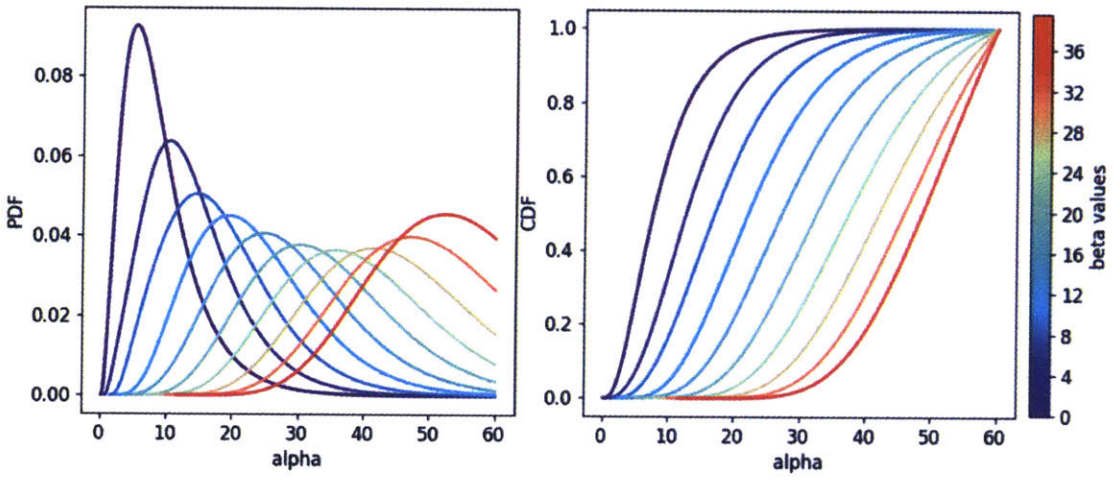

Figure 4.3: PDFs and CDFs in α for H in H_2O and a temperature of 650 K, for various β values.

The methods described in Algorithm 1 require construction of the α CDF to be specific to a given incoming neutron energy E, as it dictates the values of $\alpha_{\min}$ and $\alpha_{\max}$. As discussed in Sec. 1.4.3, this would be undesirable as it would greatly increase the required memory. So the latter method discussed in Sec. 1.4.3 is used, which does not discriminate against non-physical α values during CDF construction,

$$\hat{h}(\alpha|\beta,T) = \frac{S_{n.sym}(\alpha,\beta,T)}{\int_0^{\alpha_\infty} S_{n.sym}(\alpha',\beta,T)d\alpha'} \tag{1.72}$$

$$\hat{H}(\alpha|\beta,T) = \int_0^{\alpha} \hat{h}\left(\alpha'|\beta,T\right) d\alpha' \tag{1.73}$$

and later compensates for the non-physical values,

$$H(\alpha|\beta,E,T) = \frac{\hat{H}(\alpha|\beta,T) - \hat{H}(\alpha_{\min}|\beta,T)}{\hat{H}(\alpha_{\max}|\beta,T) - \hat{H}(\alpha_{\min}|\beta,T)}. \tag{1.74}$$

Algorithm 2 Calculate α CDF while considering full α grid

Given: Defined $\alpha_{vec}, \beta_{vec}, E, T, S_{n.sym}(\alpha,\beta)$
for T in Temperatures **do**
  Area = Integrate $S_{n.sym}(\alpha,\beta,T)$ from $\alpha_0 \rightarrow \alpha_\infty$
  for α in α_{vec} **do**
    $\hat{h}(\alpha|\beta,T) = S_{n.sym}(\alpha,\beta,T))$/Area
    $\hat{H}(\alpha|\beta,T) = \hat{H}(\alpha-1|\beta,T) + \hat{h}(\alpha|\beta,T)$
  end for
  $H(\alpha|\beta,E,T) = \left(\hat{H}(\alpha|\beta,T) - \hat{H}(\alpha_{\min}|\beta,T)\right) / \left(\hat{H}(\alpha_{\max}|\beta,T) - \hat{H}(\alpha_{\min}|\beta,T)\right)$
end for

Employing Algorithm 2 results in an identical CDF to that presented in Fig. 4.2, and is thus not plotted.

4.1.2 PDF and CDF in β

In addition to the α PDFs and CDFs, the β PDFs and CDFs are also constructed, using Eqs. 1.68,1.70,

$$g(\beta|E,T) = \frac{\int_{\alpha_{\min}}^{\alpha_{\max}} S_{n.sym}(\alpha',\beta,T)\ d\alpha'}{\int_{\beta_{\min}}^{\beta_{\max}} \int_{\alpha_{\min}}^{\alpha_{\max}} S_{n.sym}(\alpha',\beta',T)d\alpha'\ d\beta'} \tag{1.68}$$

$$G(\beta|E,T) = \int_{\beta_{\min}}^{\beta} g\left(\beta'|E,T\right) d\beta'. \tag{1.70}$$

PDFs and CDFs in β are shown in Figs. 4.4-4.5, respectively, where an α spanning $0.01 \leq \alpha \leq 60.0$ with equal spacing $\Delta\alpha \approx 0.12$ is used, along with a β mesh spanning $0.0 \leq \beta \leq 40.0$ with equal spacing $\Delta\beta \approx 0.404$.

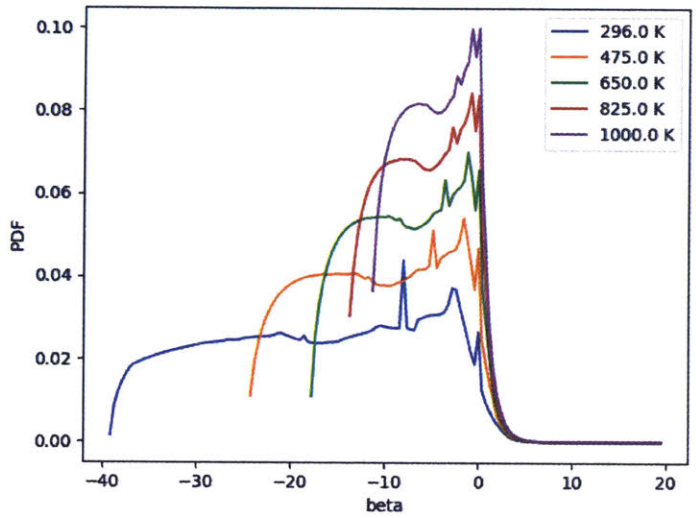

Figure 4.4: PDF in β for H in H_2O, given $E = 10.0$ eV, for various temperatures. The scattering laws used to plot these distributions were generated using the translated version of LEAPR.

4.1.3 Effect of Temperature on PDFs and CDFs

As can be seen in Figs. 4.1-4.5, the PDFs and CDFs in α and β are very sensitive to changes in material temperature. This dependence is further explored and presented in this section. Fig. 4.6 shows the effect of temperature on α CDFs, for 20 different α values. As was the case for Figs. 4.1-4.2, a β value of 10.1 is used to generate the CDFs. Note that in the α regions where the CDF values are the most temperature dependent ($20 \leq \alpha \leq 30$), an increase in temperature returns a steady increase in CDF.

The temperature dependence of the β CDF is shown in Fig. 4.7. As was the case in Figs. 4.4-4.5, an initial value $E = 10.0$ eV is assumed. Note that for many negative values of β, the CDF plot does not extend to higher temperatures - this is because the minimum realistic β value is $-E/k_bT$, since that corresponds with a neutron losing all its energy.

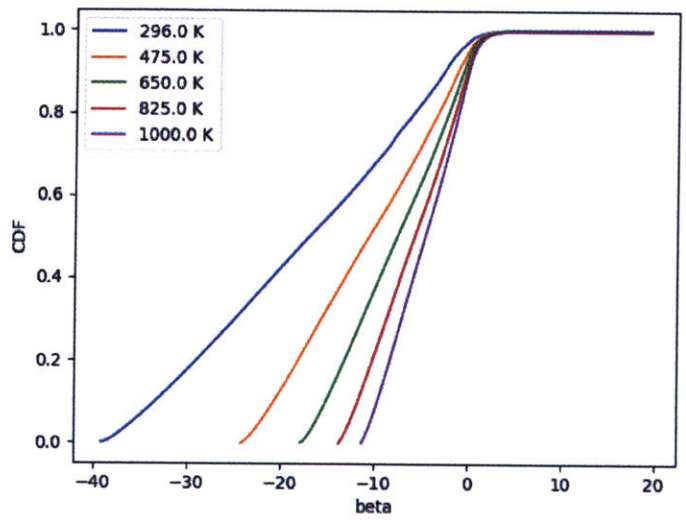

Figure 4.5: CDF in β for H in H_2O, given $E = 10.0$ eV, for various temperatures. The scattering laws used to plot these distributions were generated using the translated version of LEAPR.

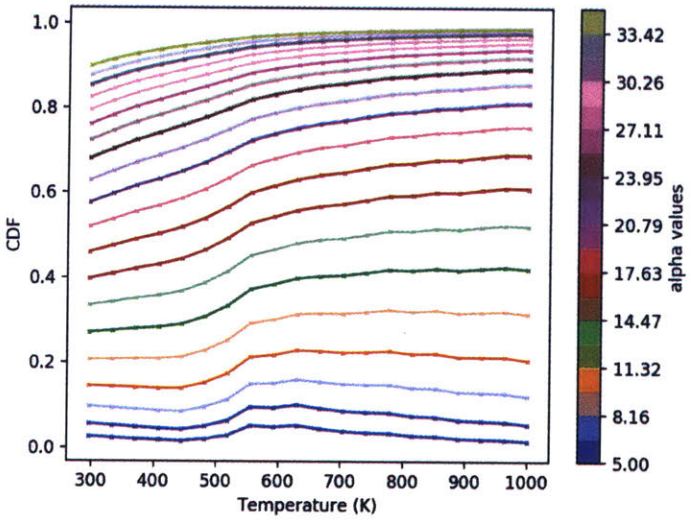

Figure 4.6: Effect of Temperature on α CDFs, for various α values. These CDFs were generated using a β value of 10.1.

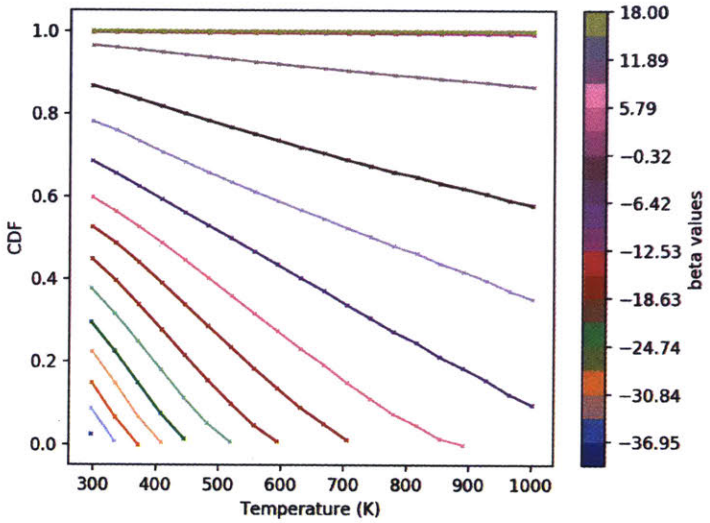

Figure 4.7: Effect of Temperature on β CDFs, for various β values. These CDFs were generated assuming an incoming energy value of $E = 10.0$ eV.

4.2 Example of Sampling β from CDF

The α and β PDFs and CDFs for H in H_2O were presented in Sec. 4.1, and can be used to sample α and β values, using the process described in Sec. 1.4. In this section, the process of sampling a β value is detailed.

For this discussion, we consider room temperature ($T = 0.0255$ eV) water, and an incident neutron with energy $E = 0.0255$ eV. The smallest β value possible is $-E/k_bT = -1$, which corresponds to complete loss of neutron energy ($E' = 0$). The maximum β value is considered to be cut off at $\beta = 20.0$ (following the convention used in [10]), which corresponds to the neutron leaving the collision with a final energy $E' = 0.5355$ eV. This is the β range that will be used in the remainder of this example.

These three key β values are listed in Table 4.1, along with their bounding α values. The minimum α value is $\alpha_{\text{min}} = 0$, which occurs when $\beta = 0$, while the maximum α value is $\alpha_{\text{max}} = 31.1910$, which occurs for a $\beta = 20.0$. Thus, for the β range of $-1 \leq \beta \leq 20$, an α range of $0 \leq \alpha \leq 32$ will suffice. For this example, very fine α, β grids were used, with 100 and 1000 points used in their grids, respectively.

	$\beta_{\text{min}} = -1.0$	$\beta = 0$	$\beta_{\text{max}} = 20.0$
α_{min}	1.0008	0.000	12.8455
α_{max}	1.0008	4.003	31.1910

Table 4.1: Bounding α values for the chosen β range. The minimum and maximum α values for a given β value are defined by Eq. 1.61.

NJOY's LEAPR module stores the $-\beta$ side of the non-symmetric scattering law, $S_{n.sym}(\alpha, -\beta)$, because its values tend to be of more reasonable size, and thus are easier to accurately store. This output is plotted in Fig. 4.8 against β, for various α values. Note that the β grid extends from $0 \rightarrow 20$, meaning that $S_{n.sym}(\alpha, \beta = 0) \rightarrow S_{n.sym}(\alpha, \beta = -20)$ is plotted. Although $\beta_{\text{min}} = -1$ for this example (and thus $\beta = -20$ will not be used in calculations), a β value of -20.0 is still required so as to retrieve the $\beta = 20.0$ value, which will be used in calculations.

Eq. 1.26 can be used to relate positive and negative sides of the non-symmetric scattering law,

$$S_{sym}(\alpha, \beta, T) = e^{\beta/2} S_{n.sym}(\alpha, \beta, T), \tag{1.26}$$

by starting with the symmetric form of the scattering law, and converting it to the non-symmetric form

$$S_{sym}(\alpha, \beta, T) = S_{sym}(\alpha, -\beta, T) \tag{4.1}$$

$$e^{\beta/2}\ S_{n.sym}(\alpha, \beta, T) = e^{-\beta/2}\ S_{n.sym}(\alpha, -\beta, T) \tag{4.2}$$

$$S_{n.sym}(\alpha, \beta, T) = e^{-\beta}\ S_{n.sym}(\alpha, -\beta, T). \tag{4.3}$$

Thus, the $+\beta$ side of the non-symmetric scattering law obtained by multiplying the $-\beta$ side by an exponential in β. Note that this will result in extremely small values of

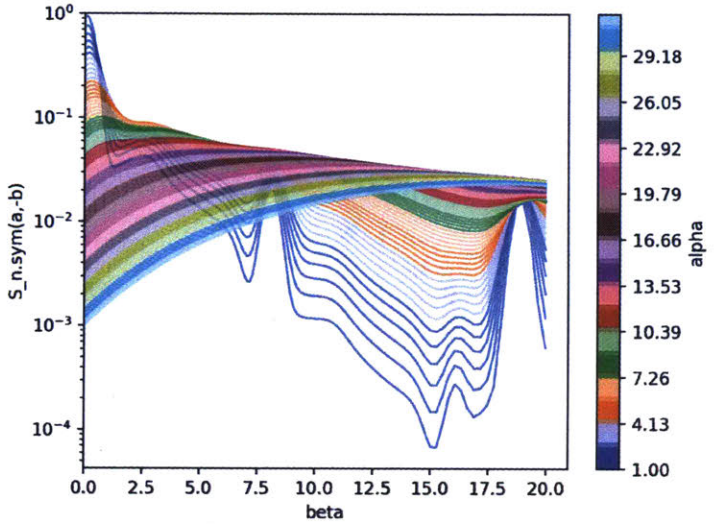

Figure 4.8: The $-\beta$ side of the non-symmetric form of the scattering law, $S_{n.sym}(\alpha, -\beta)$ is shown above. This was generated using an input based off of NJOY's Test #9 input [3].

$S_{n.sym}(\alpha, \beta)$ (and illustrates why storing the $-\beta$ side is the preferred method). The full non-symmetric scattering law is plotted in Fig. 4.9.

Using the scattering law from Fig. 4.9, the β PDF can be constructed using Eq. 1.68,

$$g(\beta|E,T) = \frac{\int_{\alpha_{\min}}^{\alpha_{\max}} S_{n.sym}(\alpha', \beta, T)\ d\alpha'}{\int_{\beta_{\min}}^{\beta_{\max}} \int_{\alpha_{\min}}^{\alpha_{\max}} S_{n.sym}(\alpha', \beta', T) d\alpha'\ d\beta'} \tag{1.68}$$

as was done in Sec. 4.2. The resultant PDF and CDF are shown in Fig. 4.10. Notice that unlike Fig. 4.9, the minimum β value shown is the physically meaningful value of -1 that was discussed in the beginning of this section. The most obvious feature of Fig. 4.10 is that large values of β (i.e. $\beta > 5$) are extremely unlikely, according to the PDF. This is in agreement with the scattering law plotted in Fig. 4.9, which shows that for $\beta > 5$, the scattering law is on the order of 10^{-5} or below, despite being on the order of 0.1 when $\beta = 0$. This supports the notion that $\beta = 20.0$ is a reasonable cutoff, since large gains in neutron energy are so unlikely.

The β CDF is sampled using the sampling technique detailed in Sec. 1.4 [10], and the scattering kernel (for a neutron of incoming energy $E = 0.0255$ eV) is plotted in Fig. 4.11. Note that the edge of the plateau near $E' = 0.02$ eV is indicative of no energy change. The increased probability on the low E' region (near $E' = 4 \times 10^{-5}$ eV) corresponds to a $\beta = -0.998$, which is very near the minimum β value.

This example can be extended to include sampling in α, but for the sake of brevity is not included here.

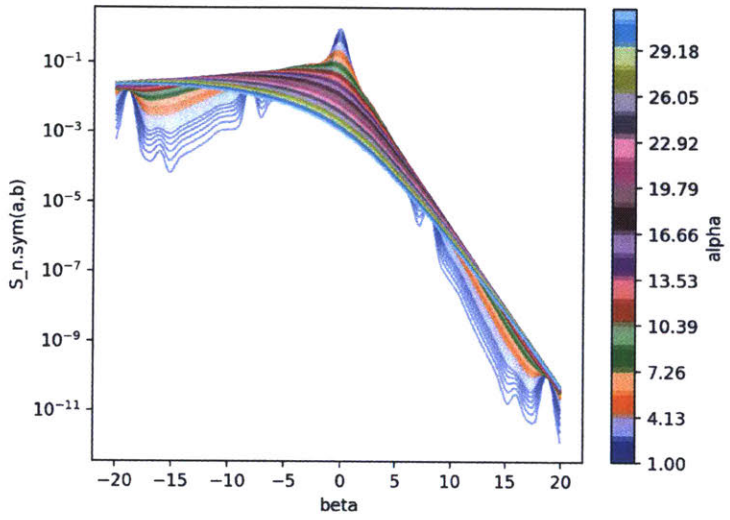

Figure 4.9: $S_{n.sym}(\alpha, \beta)$ is plotted for $\beta = -20 \rightarrow 20$. This was obtained by using Eq. 4.3 to convert the $S_{n.sym}(\alpha, -\beta)$ from Fig. 4.8 to $S_{n.sym}(\alpha, \beta)$. Note that while this shows β values extending to -20, the $\beta_{\text{min}} = -1$ is still the lowest β value with physical significance for the present example.

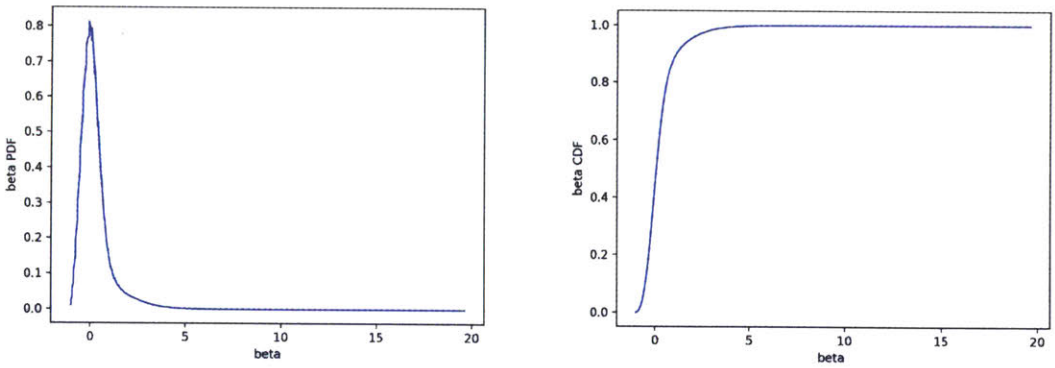

Figure 4.10: The β PDF and CDF for water at room temperature are shown above, having been constructed using the $S_{n.sym}(\alpha, \beta)$ plotted in Fig. 4.9. Note that β values quite near to zero are most likely (i.e. extreme cases of upscattering are very unlikely).

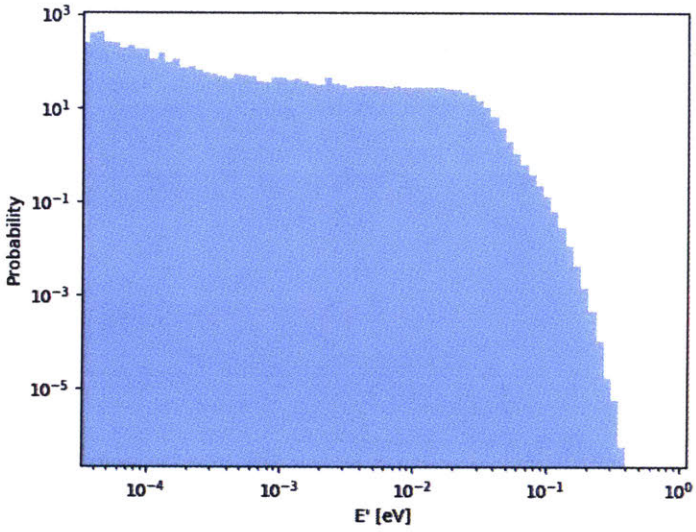

Figure 4.11: The scattering kernel for H in H_2O, which is obtained by using the β CDF sampling technique detailed in Sec. 1.4, is shown above. An initial energy of $E = 0.0255$ eV is assumed.

Chapter 5

Improvements to Numerical Methods

The LEAPR module of NJOY is a popular and trusted tool for preparing thermal neutron scattering data. It includes, however, a significant number of unnecessary approximations and antiquated numerical methods. Perhaps the most striking approximation is the discrete oscillator approximation, which has already been discussed at length in Sec. 3. This section aims to address two less major (but still certainly significant) shortcomings in the NJOY LEAPR code, and both pertain to the phonon expansion. The first is the existence of redundant operations, and the second is the arbitrary summation limits.

A brief reminder of the phonon expansion is provided, since both shortcomings pertain to this calculation. Recall that in Sec. 1.3, the phonon expansion was introduced,

$$S^{(s)}_{n.sym}(\alpha,\beta,T) = \mathrm{e}^{-\alpha\lambda_s}\sum_{n=0}^{\infty}\frac{1}{n!}\left[\alpha\lambda_s\right]^n \mathcal{T}_n(\beta) \tag{1.38}$$

where $\mathcal{T}_n(\beta)$ is obtained by convolving the previous function with $\mathcal{T}_1(\beta)$,

$$\mathcal{T}_n(\beta) = \int_{-\infty}^{\infty}\mathcal{T}_1\left(\beta'\right)\mathcal{T}_{n-1}\left(\beta-\beta'\right)d\beta' \tag{1.45}$$

$$\mathcal{T}_1(\beta) = \frac{P(\beta)\mathrm{e}^{-\beta/2}}{\lambda_s}. \tag{1.44}$$

Here, $P(\beta)$ is a function of β and of the frequency distribution $\rho(\beta)$, and the Debye-Waller coeffiecient λ_s is defined as

$$\lambda_s = \int_{-\infty}^{\infty}P(\beta')\mathrm{e}^{-\beta'/2}\,d\beta'. \tag{1.34}$$

5.1 Redundant Operations in Phonon Expansion

The current approach in NJOY's LEAPR module is to calculate $\mathcal{T}_1(\beta)$, add the $n=1$ contribution, convolve $\mathcal{T}_1(\beta)$ with itself to obtain $\mathcal{T}_2(\beta)$, add the $n=2$ contribution, etc.

(note that the $n = 0$ term is later accounted for). With a closer look, however, it becomes apparent that some of the operations in this calculation are not strictly necessary.

To best illustrate this, consider the calculation of $\mathcal{T}_2(\beta)$, which requires $\mathcal{T}_1(\beta)$ be convolved with itself,

$$\mathcal{T}_2(\beta) = \int_{-\infty}^{\infty} \mathcal{T}_1(\beta')\,\mathcal{T}_1(\beta-\beta')\;d\beta' \tag{5.1}$$

$$= \int_{-\infty}^{\infty} \left(\frac{P(\beta')e^{-\beta'/2}}{\lambda_s}\right)\left(\frac{P(\beta-\beta')\mathrm{e}^{-(\beta-\beta')/2}}{\lambda_s}\right)\;d\beta' \tag{5.2}$$

$$= \frac{\mathrm{e}^{-\beta/2}}{\lambda_s^2}\int_{-\infty}^{\infty} P(\beta')P(\beta-\beta')\;d\beta'. \tag{5.3}$$

Here, we find that the Debye-Waller coefficients, as well as the exponential factor, can be removed from the integral, leaving $\mathcal{T}_2(\beta)$ in a simpler form. Continuing with the calculation of $\mathcal{T}_3(\beta)$, we convolve $\mathcal{T}_1(\beta)$ with $\mathcal{T}_2(\beta)$,

$$\mathcal{T}_3(\beta) = \int_{-\infty}^{\infty} \mathcal{T}_1(\beta')\,\mathcal{T}_2(\beta-\beta')\;d\beta' \tag{5.4}$$

$$= \int_{-\infty}^{\infty} \left(\frac{P(\beta')\mathrm{e}^{-\beta'/2}}{\lambda_s}\right)\left(\frac{\mathrm{e}^{-(\beta-\beta')/2}}{\lambda_s^2}\int_{-\infty}^{\infty} P(\beta'')P((\beta-\beta')-\beta'')\;d\beta''\right)\;d\beta' \tag{5.5}$$

$$= \frac{\mathrm{e}^{-\beta/2}}{\lambda_s^3}\int_{-\infty}^{\infty} P(\beta')\int_{-\infty}^{\infty} P(\beta'')P(\beta-\beta'-\beta'')\;d\beta''\;d\beta', \tag{5.6}$$

a pattern becomes apparent. Instead of convolving $\mathcal{T}_1(\beta)$ with $\mathcal{T}_{n-1}(\beta)$, we can define a new set of functions

$$W_n(\beta) = \int_{-\infty}^{\infty} P(\beta')W_{n-1}(\beta-\beta')\;d\beta' \tag{5.7}$$

where

$$W_1(\beta) = P(\beta), \tag{5.8}$$

such that these $W_n(\beta)$ functions are related to the standard $\mathcal{T}_n(\beta)$ by

$$\mathcal{T}_n(\beta) = \frac{\mathrm{e}^{-\beta/2}}{\lambda_s^n}\,W_n(\beta). \tag{5.9}$$

This new representation using $W_n(\beta)$ makes it clear that, when $\mathcal{T}_n(\beta)$ is used in the Eq. 1.38, the number of operations necessary can be significantly reduced. This is because the λ_s terms cancel out, and the exponential in β needs to be solved for only once, as shown in Eq. 5.11.

$$S^{(s)}_{n.sym}(\alpha,\beta,T) = \mathrm{e}^{-\alpha\lambda_s}\sum_{n=0}^{\infty}\frac{1}{n!}\left[\alpha\lambda_s\right]^n\left[\frac{1}{\lambda_s^n}\mathrm{e}^{-\beta/2}\,W_n(\beta)\right] \tag{5.10}$$

$$S^{(s)}_{n.sym}(\alpha,\beta,T) = \mathrm{e}^{-\alpha\lambda_s-\beta/2}\sum_{n=0}^{\infty}\frac{\alpha^n}{n!}\,W_n(\beta) \tag{5.11}$$

5.2 Summation Limits for Phonon Expansion

When LEAPR calculates Eq. 1.38, it approximates the infinite sum to an arbitrary number of terms (specified by user, with a default value of $n = 100$). This cutoff is an arbitrary choice, and in this section we discuss potential consequences of using default limits for this sum.

Recall again the primary equation of the phonon expansion,

$$S^{(s)}_{n.sym}(\alpha, \beta, T) = \mathrm{e}^{-\alpha\lambda_s} \sum_{n=0}^{\infty} \frac{1}{n!} [\alpha\lambda_s]^n \mathcal{T}_n(\beta) \tag{1.38}$$

where it is immediately clear that the sum's convergence will depend on α. To investigate this dependence, consider a β grid that extends from 0.0 to 20.0 (with a spacing of 0.01), along with the phonon grid from NJOY's Test #9 (which was introduced in Sec. 3.1.1). The total contribution to $S^{(s)}_{n.sym}(\alpha, \beta)$ from the n^{th} term for a given α is defined as

$$C(\alpha, n) = \sum_{\beta} \mathrm{e}^{-\alpha\lambda_s} \frac{1}{n!} [\alpha\lambda_s]^n \mathcal{T}_n(\beta) \tag{5.12}$$

for a fixed temperature. These contributions are calculated and plotted against n for various values of α in Fig. 5.1, for a temperature of 293 K (0.025 eV). Note that for small

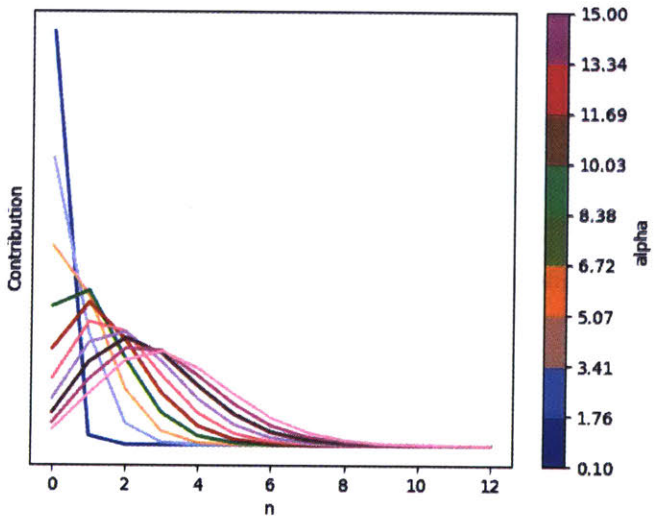

Figure 5.1: The convergence of $S(\alpha, \beta)$ acrose terms of the phonon expansion is shown. The total contribution $C(\alpha, n)$ defined in Eq. 5.12 is plotted against summation number n for various α values. All plots are normalized so as to facilitate comparison of convergence.

α (e.g. $\alpha = 0.1$) the contributions to the phonon expansion are negligibly small by the

2^{nd} term, whereas for larger α values (e.g. $\alpha = 15.0$) meaningful contributions are made up to the 10^{th} term.

Temperature is found to have an impact on the convergence of the phonon expansion contributions[1], so this effect is further explored in Fig. 5.2, for an α value of 10.0.

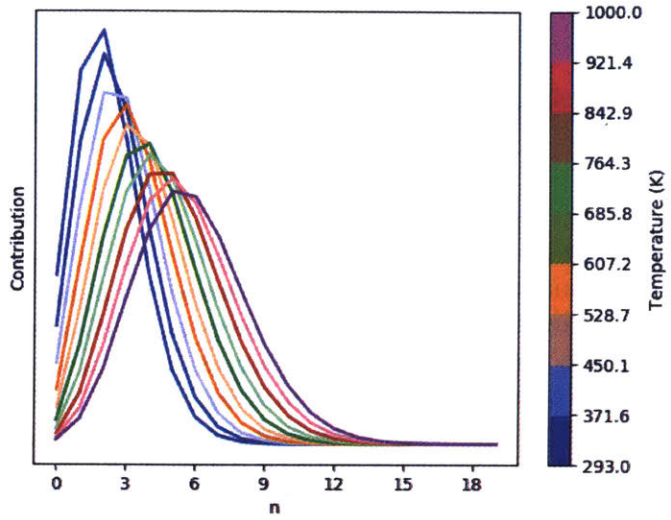

Figure 5.2: The convergence of $S(\alpha, \beta)$ across terms of the phonon expansion is shown, for a fixed α value of 10.0. The effect of temperature on convergence is explored by using ten temperatures between 293 K and 1000 K. As before, the total contribution $C(\alpha, n)$ defined in Eq. 5.12 is plotted against summation number n, and all plots are normalized so as to facilitate comparison of convergence.

As temperature increases the number of terms necessary to reach convergence increases. However, the number of terms necessary tends to be relatively small (i.e. less than 20).

Clearly, different temperatures and values of α heavily influence the convergence behavior of the phonon expansion sum, suggesting that a uniform, predefined cutoff is not an appropriate approximation to computing Eq. 1.38. The most important terms in the summation (i.e. the values of n that have the largest total contribution, as defined in Eq. 5.12) increase with increasing values of α, but in this limited exploration do not seem to require 100 terms or more, for reasonable temperatures. This suggests that for a vast many applications, the $n_{\max}$ cutoff is unnecessarily high, and thus the calculation of Eq. 1.38 could be significantly sped up. Incorporation of a convergence criteria is thus suggested, and will be imposed in future development of LEAPR.

[1]The frequency distribution is provided as a function of energy change in eV, and so to use this distribution in the phonon expansion, its grid has to be converted to a β grid (where $\beta = (E - E')/k_b T$). This imposes a temperature dependence on the frequency distribution, which further affects the contributions to the scattering law.

Chapter 6

Conclusions and Further Work

Efficient access to accurate nuclear data is crucial to simulations of nuclear systems. Characterization of thermal neutrons (i.e. those with energy on the order of 1 eV or less) is particularly important, due to the role that low energy neutrons play in thermal reactors. While characterizing the way in which slow neutrons interact with molecules can be a daunting task, it is made easier by use of the scattering law $S(\alpha, \beta, T)$, which is dependent only on temperature, energy exchange, and momentum exchange. The scattering law is obtained by use of either restrictive approximations (e.g. free gas approximation) or by providing a phonon frequency spectrum. The current methods for calculating $S(\alpha, \beta)$ given a frequency spectrum are outdated and require a number of approximations and restrictions, such as the discrete oscillator approximation, the restriction to using a uniform input phonon distribution grid, and various numerical inefficiencies detailed in Sec. 2 and Sec. 5.

The most thoroughly considered approximation studied in this project was the discrete oscillator approximation, which was discussed in Sec. 3. Since the discrete approximation is a non-physical representation of the vibrational spectrum, and does not result in significant computational benefits (due to the requirement that any discrete oscillator contributions be convolved with the existing $S(\alpha, \beta, T)$), it is recommended that the discrete oscillator approximation be abandoned. There are situations, however, in which users may want to replicate scattering kernels that were generated using the discrete oscillator approximation (e.g. replication of previously acquired thermal scattering data). To support this, it was shown in Sec. 3.7 that the discrete oscillator behavior can be approached by using increasingly thin triangles in the input frequency distribution.

Representing a discrete oscillator as an extremely thin triangle in the frequency distribution could result in a prohibitively costly computation, due to the restriction that the input frequency spectrum be provided on a uniformly spaced grid. This is because the requirement that a frequency distribution be provided on a uniformly spaced grid forces that the level of detail used to describe a thin triangle be used in all other regions of the frequency distribution. This highlights another shortcoming of the current thermal scattering data preparation methods, which will be made available in future work.

Once the scattering law $S(\alpha, \beta, T)$ is constructed using a code like NJOY's LEAPR

module, it is typically used to calculate the thermal scattering kernel and written to an output file (using, for example, the THERMR NJOY module). Since the scattering cross sections are dependent on the initial neutron energy E, final neutron energy E', material temperature T, and scattering cosine μ, these output files can be extremely large. To combat prohibitively large memory usage, a fitting approach in temperature has been developed by [10], so as to eliminate the need for storing the scattering data for many different temperatures. This fitting approach in temperature has been replicated in Sec. 4.1 and is implemented in the OpenMC Monte Carlo transport code for further validation [16].

Future work will include continued improvement of LEAPR, transition to non-uniform input frequency distributions, and analysis into obtaining accurate frequency distributions (e.g. distributions that are temperature dependent, have fully resolved peaks as opposed to discrete oscillators, etc.). Additionally, analysis into other approximations used by LEAPR and THERMR, such as the diffusive model for liquids and gasses, the free gas approximation, and the short collision time approximation, would be beneficial to the nuclear data community.

Bibliography

[1] M Herman, Cross Sections Evaluation Working Group, et al. *ENDF-6 Formats Manual Data Formats and Procedures for the Evaluated Nuclear Data File ENDF/B-VI and ENDF/B-VII.* Tech. rep. Brookhaven National Laboratory (BNL) National Nuclear Data Center, 2009.

[2] *ADS Nuclear Data Library. ACE formatted Library for Accelerator Driven Systems.* https://www-nds.iaea.org/adsV1/adsace.html. [Online; accessed 7-December-2017]. 2005.

[3] Robert Macfarlane et al. *The NJOY Nuclear Data Processing System, Version 2016.* Tech. rep. Los Alamos National Laboratory (LANL), 2017.

[4] Jesse Curtis Holmes. "Monte Carlo Calculation of Thermal Neutron Inelastic Scattering Cross Section Uncertainties by Sampling Perturbed Phonon Spectra". PhD thesis. North Carolina State University, 2014.

[5] Michael Maurice Rudolph Williams. "The slowing down and thermalization of neutrons". In: (1966).

[6] Donald E Parks et al. *Slow neutron scattering and thermalization with reactor applications.* New York: W.A. Benjamin, 1970.

[7] Léon Van Hove. "Correlations in Space and Time and Born Approximation Scattering in Systems of Interacting Particles". In: *Phys. Rev.* 95 (1 1954), pp. 249–262. DOI: 10.1103/PhysRev.95.249. URL: https://link.aps.org/doi/10.1103/PhysRev.95.249.

[8] George I Bell and Samuel Glasstone. *Nuclear reactor theory.* Tech. rep. US Atomic Energy Commission, Washington, DC (United States), 1970.

[9] K Sturm. "Dynamic structure factor: An introduction". In: *Zeitschrift für Naturforschung A* 48.1-2 (1993), pp. 233–242.

[10] Andrew T Pavlou and Wei Ji. "On-the-fly sampling of temperature-dependent thermal neutron scattering data for Monte Carlo simulations". In: *Annals of Nuclear Energy* 71 (2014), pp. 411–426.

[11] George H Vineyard. "Scattering of slow neutrons by a liquid". In: *Physical Review* 110.5 (1958), p. 999.

[12] JI Marquez Damian, JR Granada, and DC Malaspina. *CAB models for water: a new evaluation of the thermal neutron scattering laws for light and heavy water in ENDF-6 format.* Tech. rep. 2014, pp. 280–289.

[13] PA Egelstaff and P Schofield. "On the evaluation of the thermal neutron scattering law". In: *Nuclear Science and Engineering* 12.2 (1962), pp. 260–270.

[14] Aleksandar Ivanonv. "Temperature dependence correction methodology for discrete and continuous bound hydrogen in H2O thermal neutron scattering data". In: *Annals of Nuclear Energy* 102 (2017), pp. 402–407.

[15] Clinton T Ballinger. "The direct S (α, β) method for thermal neutron scattering". In: *Proceedings of the international conference on mathematics and computations, reactor physics, and environmental analyses. Volume 1 and 2.* 1995.

[16] Paul K Romano et al. "OpenMC: A state-of-the-art Monte Carlo code for research and development". In: *SNA+ MC 2013-Joint International Conference on Supercomputing in Nuclear Applications+ Monte Carlo.* EDP Sciences. 2014, p. 06016.

[17] David A Brown et al. "ENDF/B-VIII. 0: the 8th major release of the nuclear reaction data library with CIELO-project cross sections, new standards and thermal scattering data". In: *Nuclear Data Sheets* 148 (2018), pp. 1–142.

[18] Ankit Rohatgi. *WebPlotDigitizer.* 2011.

[19] VA Babenko and NM Petrov. "Determination of low-energy parameters of neutron-proton scattering on the basis of modern experimental data from partial-wave analyses". In: *Physics of Atomic Nuclei* 70.4 (2007), pp. 669–675.

[20] JU Koppel and DH Houston. *REFERENCE MANUAL FOR ENDF THERMAL NEUTRON SCATTERING DATA.* Tech. rep. Gulf General Atomic, Inc., San Diego, Calif., 1968.

Appendices

Appendix A

Background

A.1 Incoherent Approximation

As mention in Sec. 1.2.1, the differential scattering cross section is comprised of a coherent and an incoherent part. Coherent scattering accounts for interference between scattered waves, while incoherent scattering consists as a sum of non-interacting waves. The coherent contribution to the cross section is crucial to describing elastic scattering, as well as inelastic scattering for single-crystal materials. For polycrystalline solids and for liquids, however, interference effects are often neglected in what is called the "incoherent approximation" [5]. The validity of this approximation is now explored, for the simple case of a predominantly hydrogenous material.

A.1.1 Relating Scattering Lengths to Cross Sections

The bound scattering cross sections σ_{coh} and σ_{inc} must account for the total spin of the nucleus-neutron system. Since the neutron has spin $\frac{1}{2}$, the total spin is either $I + \frac{1}{2}$ or $I - \frac{1}{2}$, given the nucleus has spin I. Thus, the bound incoherent and coherent scattering cross sections are defined as

$$a_{inc}^2 = \sum_i^N p_i \left[\frac{I_i + 1}{2I_i + 1} \left(a_i^+\right)^2 + \frac{I_i}{2I_i + 1} \left(a_i^-\right)^2 \right] - a_{coh}^2 \tag{A.1}$$

and

$$a_{coh}^2 = \sum_i^N p_i \left[\frac{I_i + 1}{2I_i + 1} a_i^+ + \frac{I_i}{2I_i + 1} a_i^- \right]^2 \tag{A.2}$$

for a system consisting of N isotopes with abundance p_i, where the bound scattering amplitudes $a_i^{\pm}$ correspond to total spins of $I_i \pm \frac{1}{2}$ [5]. The $I_i \pm \frac{1}{2}$ spin states occur with probability $(I+1)/(2I+1)$ and $I/(2I+1)$, respectively. Thus, Eq. A.2 can be interpreted as the first central moment of the scattering amplitude $\langle a \rangle$.

$$a_{coh} = \langle a \rangle \tag{A.3}$$

Similarly, the incoherent scattering length can be seen as the second central moment of the scattering length [8]

$$a_{inc} = \langle a^2 \rangle - \langle a \rangle^2. \tag{A.4}$$

A.1.2 Bound Scattering Cross Sections for Hydrogen

Consider a material whose dominant element is H-1, which has a nuclear spin of $\frac{1}{2}$. If the proton is hit by a neutron, the proton-neutron system can form either a singlet state or a triplet state, which have total spin $S^- = 0$ and $S^+ = 1$, respectively. The singlet state occurs with multiplicity 1 and has a scattering length $a^- = -23.748$ fm, while the triplet state occurs with multiplicity 3 and has a scattering length $a^+ = 5.424$ fm [19]. As seen in Eqs. A.1, A.2, the coherent and incoherent bound cross sections depend on the average values of a and a^2. Computing these values simply requires weighting a^- and a^+ by their multiplicities.

$$\langle a \rangle = \left(\frac{3}{4} a^+ + \frac{1}{4} a^- \right) = -1.869 \text{ fm} \tag{A.5}$$

$$\langle a^2 \rangle = \left(\frac{3}{4} \left(a^+ \right)^2 + \frac{1}{4} \left(a^- \right)^2 \right) = 163.1 \text{ fm}^2 \tag{A.6}$$

So the coherent and incoherent bound scattering cross sections are thus

$$\sigma_{coh} = 4\pi \langle a \rangle^2 = 0.439 \text{ b} \tag{A.7}$$

and

$$\sigma_{inc} = 4\pi \left(\langle a^2 \rangle - \langle a \rangle^2 \right) = 20.05 \text{ b}. \tag{A.8}$$

The relative sizes of the coherent and incoherent bound scattering cross sections indicate that, due to the singlet state's negative scattering length, incoherent scattering in hydrogen has a significantly larger impact than coherent scattering in hydrogen. Thus, for hydrogenous systems, the incoherent approximation is considered acceptable.

A.2 $\mathcal{T}_n(\beta)$ Representation as a Convolution Integral

In the phonon expansion described in Sec. 1.3.1, the $\mathcal{T}_n(\beta)$ equations are stated to be the result of an iterative calculation, where the n^{th} function is the convolution between the first term and the $(n-1)^{th}$ term. This section serves to illustrate the validity of that statement.

Eqs. 1.37,1.38 define $\mathcal{T}_n(\beta)$ to be defined as

$$\mathcal{T}_n(\beta) = \frac{1}{2\pi} \frac{1}{\lambda_s^n} \int_{-\infty}^{\infty} e^{i\beta\hat{t}} \left[\int_{-\infty}^{\infty} P(\beta') e^{-\beta'/2} e^{-i\beta'\hat{t}} \, d\beta' \right]^n \, d\hat{t}. \tag{A.9}$$

The β integral that is raised to the n^{th} power can be separated into two pieces: a single integral, and an integral raised to the $(n-1)^{th}$ power,

$$\mathcal{T}_n(\beta) = \frac{1}{2\pi}\frac{1}{\lambda_s^n}\int_{-\infty}^{\infty} \mathrm{e}^{-i\beta\hat{t}}\left[\int_{-\infty}^{\infty} P(\beta')\mathrm{e}^{\beta'/2}\mathrm{e}^{-i\beta'\hat{t}}\, d\beta'\right]\left[\int_{-\infty}^{\infty} P(\beta'')\mathrm{e}^{-\beta''/2}\mathrm{e}^{-i\beta''\hat{t}}\, d\beta''\right]^{n-1} d\hat{t} \tag{A.10}$$

and the order of integration can be switched so that,

$$\mathcal{T}_n(\beta) = \frac{1}{2\pi}\frac{1}{\lambda_s^n}\int_{-\infty}^{\infty}\int_{-\infty}^{\infty} \mathrm{e}^{-i\beta\hat{t}}P(\beta')\mathrm{e}^{\beta'/2}\mathrm{e}^{-i\beta'\hat{t}}\left[\int_{-\infty}^{\infty} P(\beta'')\mathrm{e}^{-\beta''/2}\mathrm{e}^{-i\beta''\hat{t}}\, d\beta''\right]^{n-1} d\hat{t}\, d\beta'. \tag{A.11}$$

Additionally, the terms without $\hat{t}$ dependence can be removed from the time integral,

$$\mathcal{T}_n(\beta) = \frac{1}{2\pi}\frac{1}{\lambda_s^n}\int_{-\infty}^{\infty} P(\beta')\mathrm{e}^{\beta'/2}\left[\int_{-\infty}^{\infty} \mathrm{e}^{i(\beta-\beta')\hat{t}}\left[\int_{-\infty}^{\infty} P(\beta'')\mathrm{e}^{-\beta''/2}\mathrm{e}^{-i\beta''\hat{t}}\, d\beta''\right]^{n-1} d\hat{t}\right] d\beta' \tag{A.12}$$

and bringing the outside factors into the β' integral, we find that

$$\mathcal{T}_n(\beta) = \int_{-\infty}^{\infty} \frac{P(\beta')\mathrm{e}^{\beta'/2}}{\lambda_s}\left[\frac{1}{2\pi\lambda_s^{n-1}}\int_{-\infty}^{\infty} \mathrm{e}^{i(\beta-\beta')\hat{t}}\left[\int_{-\infty}^{\infty} P(\beta'')\mathrm{e}^{-\beta''/2}\mathrm{e}^{-i\beta''\hat{t}}\, d\beta''\right]^{n-1} d\hat{t}\right] d\beta' \tag{A.13}$$

where the bracketed term can be readily seen to equal $\mathcal{T}_{n-1}(\beta-\beta')$, in accordance with Eq. A.9. The equation for $\mathcal{T}_n(\beta)$ thus simplifies to

$$\mathcal{T}_n(\beta) = \int_{-\infty}^{\infty} \frac{P(\beta')\mathrm{e}^{\beta'/2}}{\lambda_s}\mathcal{T}_{n-1}\left(\beta-\beta'\right) d\beta' \tag{A.14}$$

$$= \int_{-\infty}^{\infty} \mathcal{T}_1\left(\beta'\right)\mathcal{T}_{n-1}\left(\beta-\beta'\right) d\beta' \tag{1.45}$$

which is the familiar representation presented in Sec. 1.3.1.

Appendix B

Improved Sampling of $S(\alpha, \beta)$

B.1 Formulating $\sigma^{inc.}(\alpha, \beta, T)$ from $\sigma^{inc.}(E \rightarrow E', \mu, T)$

This method involves construction of PDFs and CDFs of the scattering cross section, as a function of α and β [10]. To do this, a formulation of $\sigma(\alpha, \beta, T)$ is required. This can be achieved using a Jacobian transformation,

$$\frac{\sigma^{\text{inc.}}(E \rightarrow E', \mu, T)}{\sigma^{\text{inc.}}(\alpha, \beta, T)} = \det \begin{vmatrix} \partial\alpha/\partial\mu & \partial\alpha/\partial E \\ \partial\beta/\partial\mu & \partial\beta/\partial E \end{vmatrix} \tag{B.1}$$

$$= \frac{\partial\alpha}{\partial\mu}\frac{\partial\beta}{\partial E} - \frac{\partial\beta}{\partial\mu}\frac{\partial\alpha}{\partial E}. \tag{B.2}$$

Recalling the definitions of α and β from Eqs. 1.16-1.17, the components of the above matrix can be readily found,

$$\frac{\partial\alpha}{\partial\mu} = -\frac{2\sqrt{E'E}}{Ak_bT} \tag{B.3}$$

$$\frac{\partial\alpha}{\partial E} = \frac{1}{Ak_bT} - \frac{\mu\sqrt{E'}}{Ak_bT\sqrt{E}} \tag{B.4}$$

$$\frac{\partial\beta}{\partial\mu} = 0 \tag{B.5}$$

$$\frac{\partial\beta}{\partial E} = -\frac{1}{k_bT}. \tag{B.6}$$

which, when used in Eq. B.2 yield

$$\frac{\sigma^{\text{inc.}}(E \rightarrow E', \mu, T)}{\sigma^{\text{inc.}}(\alpha, \beta, T)} = \frac{2\sqrt{E'E}}{A(k_bT)^2} \tag{B.7}$$

which shows that

$$\sigma^{\text{inc.}}(\alpha, \beta, T) = \frac{A(k_bT)^2}{2\sqrt{E'E}}\sigma^{\text{inc.}}(E \rightarrow E', \mu, T). \tag{B.8}$$

By using the definition of the cross section in Eq. 1.1, the scattering law can be incorporated into $\sigma^{inc}(\alpha,\beta,T)$,

$$\sigma^{\text{inc.}}(\alpha,\beta,T) = \frac{A(k_bT)^2}{2\sqrt{E'E}}\frac{\sigma_b}{2k_bT}\sqrt{\frac{E'}{E}}S_{n.sym}(\alpha,\beta,T) \tag{B.9}$$

which further simplifies to

$$\sigma^{\text{inc.}}(\alpha,\beta,T) = \frac{Ak_bT\sigma_b}{4E}\mathrm{e}^{-\beta/2}S_{n.sym}(\alpha,\beta,T). \tag{1.65}$$

B.2 Sampling Appropriate Region of Energy-Independent α CDF

The energy-independent PDF and CDF for α are shown in Eqs. 1.72-1.73, respectively.

$$\hat{h}(\alpha|\beta,T) = \frac{S_{n.sym}(\alpha,\beta,T)}{\int_0^{\alpha_\infty} S_{n.sym}(\alpha',\beta,T)d\alpha'} \tag{1.72}$$

$$\hat{H}(\alpha|\beta,T) = \int_0^{\alpha} \hat{h}\left(\alpha'|\beta,T\right)d\alpha' \tag{1.73}$$

By omitting the incoming neutron energy dependence, the physically meaningful bounds for α integration, $\alpha_{\min}$ and $\alpha_{\max}$, are replaced with 0 and α_∞. This allows for invalid α,β pairs (i.e. pairs that do not comply with the restrictions stated in Eq. 1.61). To counteract this, the energy-dependent CDF in Eq. 1.71 will be rewritten in terms of the energy-independent CDF in Eq. 1.73.

$$h(\alpha|\beta,E,T) = \frac{S_{n.sym}(\alpha,\beta,T)}{\int_{\alpha_{\min}}^{\alpha_{\max}} S_{n.sym}(\alpha',\beta,T)d\alpha'} \tag{1.69}$$

$$H(\alpha|\beta,E,T) = \int_{\alpha_{\min}}^{\alpha} h\left(\alpha'|\beta,E,T\right)d\alpha' \tag{1.71}$$

Inserting Eq. 1.69 into Eq. 1.71, we get

$$H(\alpha|\beta,E,T) = \int_{\alpha_{\min}}^{\alpha} \frac{S_{n.sym}(\alpha',\beta,T)}{\int_{\alpha_{\min}}^{\alpha_{\max}} S_{n.sym}(\alpha'',\beta,T)d\alpha''}d\alpha'. \tag{B.10}$$

Note that the denominator has no α' dependence, thus it is moved from the integral

$$H(\alpha|\beta,E,T) = \frac{\int_{\alpha_{\min}}^{\alpha} S_{n.sym}(\alpha',\beta,T)d\alpha'}{\int_{\alpha_{\min}}^{\alpha_{\max}} S_{n.sym}(\alpha'',\beta,T)d\alpha''}, \tag{B.11}$$

and, by manipulating the bounds of the integral, turned into

$$H(\alpha|\beta,E,T) = \frac{\int_0^{\alpha} S_{n.sym}(\alpha',\beta,T)d\alpha' - \int_0^{\alpha_{\min}} S_{n.sym}(\alpha',\beta,T)d\alpha'}{\int_0^{\alpha_{\max}} S_{n.sym}(\alpha'',\beta,T)d\alpha'' - \int_0^{\alpha_{\min}} S_{n.sym}(\alpha'',\beta,T)d\alpha''}, \tag{B.12}$$

Note that the integrals in Eq. B.12 resemble the form of Eq. 1.73, allowing it to be rewritten as

$$H(\alpha|\beta,E,T) = \frac{\hat{H}(\alpha|\beta,T) - \hat{H}(\alpha_{\min}|\beta,T)}{\hat{H}(\alpha_{\max}|\beta,T) - \hat{H}(\alpha_{\min}|\beta,T)} \tag{1.74}$$

Appendix C

Accurate Representation of Phonon Distribution

C.1 Equivalence of Revised-LEAPR to Legacy-LEAPR

NJOY's LEAPR module was translated from Fortran to C++, so as to provide flexibility in later analysis. To use the translated code for analysis requires confidence that it adequately replicates the behavior of the legacy code. Fig. 3.4 shows the $S_{n.sym}(\alpha, \beta)$ as calculated by the original LEAPR code (the translated code mimics the original code's output quite well, and thus the individual plots cannot be visually differentiated from each other).

Fig. C.2 shows the percent error and the absolute error between the $S_{n.sym}(\alpha, \beta)$ values produced by the translated and original LEAPR. Notice that the percent error is significantly lower in the β regions where $S_{n.sym}(\alpha, \beta)$ is of reasonable size. Thus, the translated version of LEAPR is considered an adequate tool for processing thermal data for the following discussion. Note that the translated LEAPR was also tested against legacy LEAPR with other cases considered, and any conclusions drawn using the translated LEAPR will be verified alongside those drawn from the legacy LEAPR.

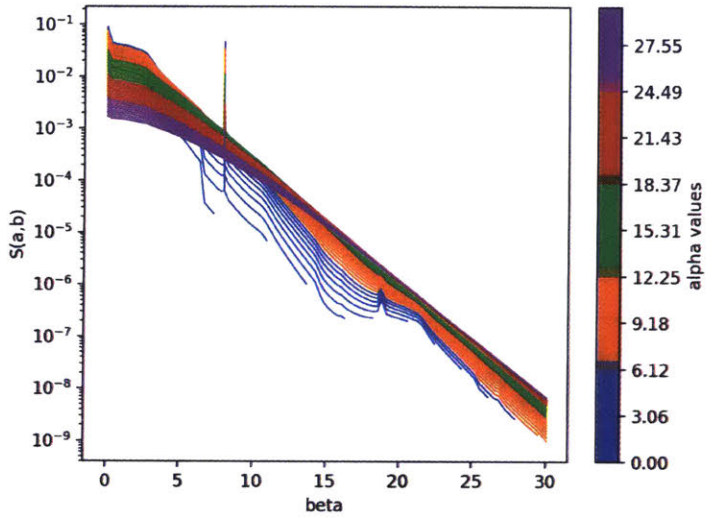

Figure 3.4: The legacy LEAPR and translated LEAPR are visually indistinguishable for the simple H in H_2O model introduced in Sec. 3.1.1, so only the former is shown. Note the sharp peak t Translated and legacy LEAPR are represented using dotted and dashed lines, respectively. Note the sharp peaks that characterize the $S_{n.sym}(\alpha, \beta)$ spectrum, which correspond to the summation values in Eq. 1.57, and are identified in Table 3.3.

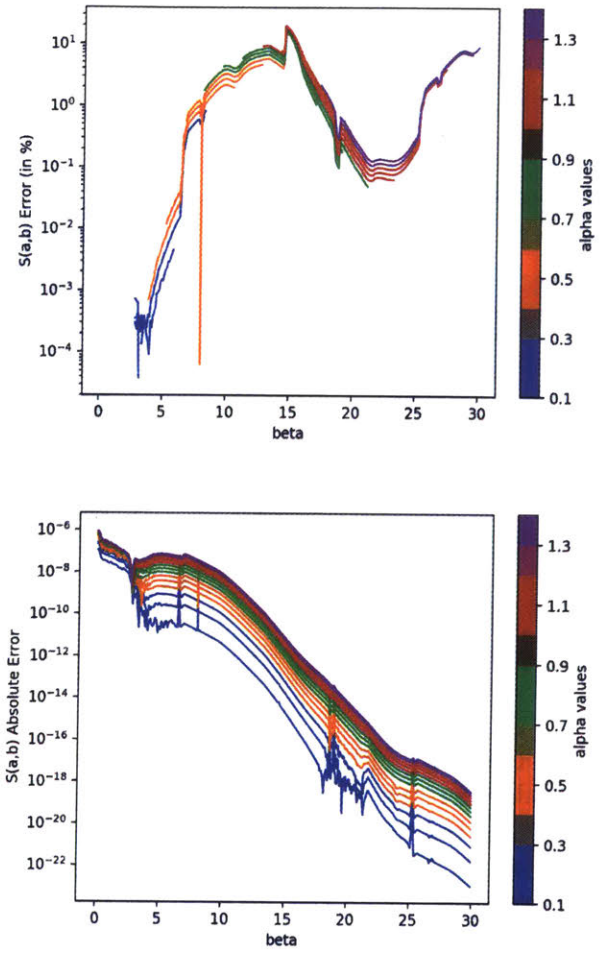

Figure C.2: Comparison of translated vs. legacy LEAPR, for Test #9, with the percent error plotted on the left side, and the absolute error plotted on the right. Note that the very large ($\sim$ 10%) errors are a direct result of the small $S_{n.sym}(\alpha, \beta)$ values, and not due to significant discrepancy between the codes' output.

C.2 Derivation of Discrete Oscillator Formulation

Recall the definition of the non-symmetric scattering law,

$$S_{n.sym}(\alpha,\beta,T) = \frac{1}{2\pi}\int_{-\infty}^{\infty} \mathrm{e}^{i\beta\hat{t}}\mathrm{e}^{-\gamma(\hat{t})}\,d\hat{t} \tag{1.27}$$

where

$$\gamma(\hat{t}) = \alpha\int_{-\infty}^{\infty} P(\beta)\left[1-\mathrm{e}^{-i\beta\hat{t}}\right]\mathrm{e}^{-\beta/2}\,d\beta \tag{1.28}$$

and

$$P(\beta) = \frac{\rho(\beta)}{2\beta\sinh(\beta/2)}. \tag{1.29}$$

Eq. 1.28 can be expanded to

$$\gamma(\hat{t}) = \alpha\int_{-\infty}^{\infty} P(\beta')\mathrm{e}^{-\beta'/2}\,d\beta - \alpha\int_{-\infty}^{\infty} P(\beta')\mathrm{e}^{-i\beta'\hat{t}}\mathrm{e}^{-\beta'/2}\,d\beta'. \tag{C.1}$$

Since $P(\beta)$ is symmetric in β, the integral in the first term can be halved to extend from $0\rightarrow\infty$,

$$\gamma(\hat{t}) = \alpha\int_{0}^{\infty} P(\beta')\left[\mathrm{e}^{\beta'/2}+\mathrm{e}^{-\beta'/2}\right]\,d\beta - \alpha\int_{-\infty}^{\infty} P(\beta')\mathrm{e}^{-i\beta'\hat{t}}\mathrm{e}^{-\beta'/2}\,d\beta', \tag{C.2}$$

and by using the definition of $P(\beta)$ from Eq. 1.29, this simplifies to

$$\gamma(\hat{t}) = \alpha\left[\int_{0}^{\infty}\frac{\rho(\beta')}{\beta'}\coth(\beta'/2)\,d\beta' - \int_{-\infty}^{\infty} P(\beta')\mathrm{e}^{-i\beta'\hat{t}}\mathrm{e}^{-\beta'/2}\,d\beta'\right]. \tag{C.3}$$

Similarly, the latter term can be expanded,

$$\int_{-\infty}^{\infty} P(\beta')\mathrm{e}^{-i\beta'\hat{t}-\beta'/2}\,d\beta' = \int_{0}^{\infty} P(\beta')\left[\mathrm{e}^{i\beta'\hat{t}}\mathrm{e}^{\beta'/2}+\mathrm{e}^{-i\beta'\hat{t}}\mathrm{e}^{-\beta'/2}\right]\,d\beta' \tag{C.4}$$

$$= \int_{0}^{\infty} P(\beta')\Big[\cos(\beta'\hat{t})\mathrm{e}^{\,\beta'/2} + i\sin(\beta'\hat{t})\mathrm{e}^{\,\beta'/2} + \tag{C.5}$$

$$\cos(\beta'\hat{t})\mathrm{e}^{-\beta'/2} - i\sin(\beta'\hat{t})\mathrm{e}^{-\beta'/2}\Big]\,d\beta' \tag{C.6}$$

$$= \int_{0}^{\infty} P(\beta')2\left[\cos(\beta'\hat{t})\cosh\left(\frac{\beta'}{2}\right) + i\sin(\beta'\hat{t})\sinh\left(\frac{\beta'}{2}\right)\right]\,d\beta', \tag{C.7}$$

and further simplified by using the facts that $\cosh(x)=\cos(ix)$ and $\sinh(x)=-i\sin(ix)$, as well as the fact that $\cos(a+b)=\cos(a)\cos(b)-\sin(a)\sin(b)$. Applying these definitions allows the bracketed part of the integrand to be rewritten as

$$\cos(\beta'\hat{t})\cosh\left(\frac{\beta'}{2}\right) + i\sin(\beta'\hat{t})\sinh\left(\frac{\beta'}{2}\right) \tag{C.8}$$

$$= \cos(\beta'\hat{t})\cos\left(\beta' i/2\right) + i\sin(\beta'\hat{t})(-i)\sin\left(\beta' i/2\right) \tag{C.9}$$

$$= \cos(\beta'\hat{t})\cos\left(\beta' i/2\right) + \sin(\beta'\hat{t})\sin\left(\beta' i/2\right) \tag{C.10}$$

$$= \cos(\beta'(\hat{t}-i/2)). \tag{C.11}$$

Inserting this simplification into Eq. C.7 shows that

$$\int_{-\infty}^{\infty} P(\beta')\mathrm{e}^{-i\beta'\hat{t}-\beta'/2}\,d\beta' = \int_{0}^{\infty} P(\beta')2\cos(\beta'(\hat{t}-i/2))\,d\beta' \tag{C.12}$$

which creates a simple expression for $\gamma(\hat{t})$,

$$\gamma(\hat{t}) = \alpha\left[\int_0^\infty \frac{\rho(\beta')}{\beta'}\coth(\beta'/2)\,d\beta' - \int_0^\infty \frac{\rho(\beta')}{\beta'\sinh(\beta'/2)}\cos(\beta'(\hat{t}-i/2))\,d\beta'\right]. \tag{C.13}$$

Thus far, no approximations have been made to the frequency distribution $\rho(\beta)$. However, now we assume that that is consists of a single discrete oscillator located at $\beta = \beta_i$ (i.e. $\rho(\beta) = \delta(\beta - \beta_i)$). This removes the integrals over β',

$$\gamma(\hat{t}) = \frac{\alpha\coth(\beta_i/2)}{\beta_i} - \frac{\alpha\cos(\beta_i(\hat{t}-i/2))}{\beta_i\sinh(\beta_i/2)}. \tag{C.14}$$

which, when plugged into Eq. 1.27, yields the non-symmetric scattering law

$$S_{n.sym}(\alpha,\beta,T) = \frac{1}{2\pi}\int_{-\infty}^{\infty}\mathrm{e}^{i\beta\hat{t}}\exp\left[-\frac{\alpha\coth(\beta_i/2)}{\beta_i} + \frac{\alpha\cos(\beta_i(\hat{t}-i/2))}{\beta_i\sinh(\beta_i/2)}\right]\,d\hat{t} \tag{C.15}$$

$$= \mathrm{e}^{-\alpha\lambda_i}\frac{1}{2\pi}\int_{-\infty}^{\infty}\mathrm{e}^{i\beta\hat{t}}\exp\left[\frac{\alpha\cos(\beta_i(\hat{t}-i/2))}{\beta_i\sinh(\beta_i/2)}\right]\,d\hat{t} \tag{C.16}$$

$$= \mathrm{e}^{-\alpha\lambda_i}\frac{1}{2\pi}\int_{-\infty}^{\infty}\mathrm{e}^{i\beta\hat{t}}\sum_{n=-\infty}^{\infty}\mathrm{I}_n\left(\frac{\alpha}{\beta_i\sinh(\beta_i/2)}\right)\mathrm{e}^{-ni(\beta_i\hat{t}-i\beta_i/2)}\,d\hat{t} \tag{C.17}$$

$$= \mathrm{e}^{-\alpha\lambda_i}\sum_{n=-\infty}^{\infty}\mathrm{I}_n\left(\frac{\alpha}{\beta_i\sinh(\beta_i/2)}\right)\mathrm{e}^{-n\beta_i/2}\frac{1}{2\pi}\int_{-\infty}^{\infty}\mathrm{e}^{i\beta\hat{t}}\mathrm{e}^{-ni\beta_i\hat{t}}\,d\hat{t} \tag{C.18}$$

$$= \mathrm{e}^{-\alpha\lambda_i}\sum_{n=-\infty}^{\infty}\mathrm{I}_n\left(\frac{\alpha}{\beta_i\sinh(\beta_i/2)}\right)\mathrm{e}^{-n\beta_i/2}\delta(\beta - n\beta_i). \tag{1.46}$$

Note that by representing the first term in Eq. C.14 as the Debye-Waller coefficient λ_i (which was originally defined in Eq. 1.47), and by introducing the modified Bessel function of the first kind $\mathrm{I}_n(x)$ in place of the large exponential in Eq. C.16, the scattering law is equal to the discrete oscillator formulation presented in Eq. 1.46 (for a single oscillator). In replacing the exponential with the Bessel function, the definition

$$\mathrm{e}^{x\cos(\theta)} = \sum_{n=-\infty}^{\infty}\mathrm{I}_n(x)\,\mathrm{e}^{-in\theta} \tag{C.19}$$

is used [20].